Journal of South American Earth Sciences 110 (2021) 103329

Contents lists available at ScienceDirect

Journal of South American Earth Sciences

journal homepage: www.elsevier.com/locate/jsames

Clay mineralogy and lithogeochemistry of lutites from the Lower Cretaceous Crato Member, Araripe Basin, NE Brazil: Implications for paleoenvironmental, paleoclimatic and provenance reconstructions

Victor Matheus Joaquim Salgado-Campos [a,b,c,*], Ismar de Souza Carvalho [a,e], Luiz Carlos Bertolino [c,d], Thamiris Agatha Duarte [a,c], Bruno Cesar Araújo [a,b], Leonardo Borghi [a,b]

[a] Universidade Federal do Rio de Janeiro, Instituto de Geociências, Departamento de Geologia, Av. Athos da Silveira Ramos, 273 - 21910-200, Cidade Universitária, Rio de Janeiro, RJ, Brazil
[b] Laboratório de Geologia Sedimentar (LAGESED), Universidade Federal do Rio de Janeiro, Instituto de Geociências, Departamento de Geologia, Av. Athos da Silveira Ramos, 273 - 21910-200, Cidade Universitária, Rio de Janeiro, RJ, Brazil
[c] Centro de Tecnologia Mineral, Coordenação de Análises Minerais, Setor de Caracterização Mineralógica, Av. Pedro Calmon, 900 - 21941-908, Cidade Universitária, Rio de Janeiro, RJ, Brazil
[d] Universidade do Estado do Rio de Janeiro, Faculdade de Geologia, Departamento de Mineralogia e Petrologia Ígnea. Rua São Francisco Xavier, 524 – 20550-000, Maracanã, Rio de Janeiro, RJ, Brazil
[e] Universidade de Coimbra, Centro de Geociências. Rua Sílvio Lia - Pólo II - 3030-709, Coimbra, Portugal

ARTICLE INFO

Keywords:
Crato Member
Aptian
Lower Cretaceous
Clay mineralogy
Lithogeochemistry
Paleoenvironment
Paleoclimate
Provenance

ABSTRACT

The Aptian Crato Member of the Araripe Basin is a 50-m-thick succession of laminated limestones alternated with siliciclastic rocks. This unit has been receiving attention worldwide mainly because it is one of the most famous fossil *Konservat-Lagerstätten*, where were identified well-preserved paleofauna and paleoflora. Clay mineralogy and lithogeochemical data have been widely used in paleoenvironmental, paleoclimatic and provenance reconstructions. However, these techniques were not systematically used to study the Crato Member rocks. This study reports the mineralogical and lithogeochemical characterization of the Crato Member lutites looking for paleoenvironmental, paleoclimatic, and provenance reconstructions. Facies analysis, X-ray diffractometry, lithogeochemical, and scanning electron microscopy studies were carried out on thirteen Crato Member lutite samples in the Três Irmãos quarry, near Nova Olinda County. Regional arid paleoclimate conditions were identified using clay mineral assemblages and two paleoenvironmental models with subtle paleoprecipitation and provenance differences were interpreted. In the lower Três Irmãos quarry, a tidal-dominated delta mouth bar facies succession coincident with a clay mineral association with lesser kaolinite contents was identified, which indicates drier conditions. Lithogeochemical data suggests provenance from Archean felsic rocks. In the upper Três Irmãos quarry, a marginal paleolagoon facies succession coincident with a clay mineral association with higher kaolinite contents was recognized, which indicates wetter conditions. Lithogeochemical data indicate provenance from mixed Post-Archean to Archean felsic-mafic rocks. The paleolagoon water was interpreted as brackish and sudden paleosalinity increases indicated seawater inputs, which were also responsible for raising the paleolagoon water table in the marginal paleolagoon facies succession, which presented paleoenvironmental proxies suggesting a more expressive marine character.

1. Introduction

The Araripe Basin is the widest and thickest interior basin of northeastern Brazil with an area of approximately 11,000 km^2 and 850 m thick (Fig. 1) (Assine, 1990, 1992; Beurlen, 1962, 1963). The Santana Formation represents part of its Aptian record and is composed of the Crato, Ipubi, and Romualdo Members (Ponte and Appi, 1990; Arai and Assine, 2020).

The Crato Member is an approximately 50-m thick succession of laminated limestones alternated with siliciclastic rocks (Assine, 2007;

* Corresponding author. Universidade Federal do Rio de Janeiro, Instituto de Geociências, Departamento de Geologia, Av. Athos da Silveira Ramos, 273 - 21910-200, Cidade Universitária, Rio de Janeiro, RJ, Brazil.
E-mail addresses: victorsalgadocampos@hotmail.com, victorsalgadocampos@ufrj.br, victorsalgadocampos@geologia.ufrj.br (V.M.J. Salgado-Campos).

https://doi.org/10.1016/j.jsames.2021.103329
Received 14 January 2021; Received in revised form 5 April 2021; Accepted 6 April 2021
Available online 15 April 2021

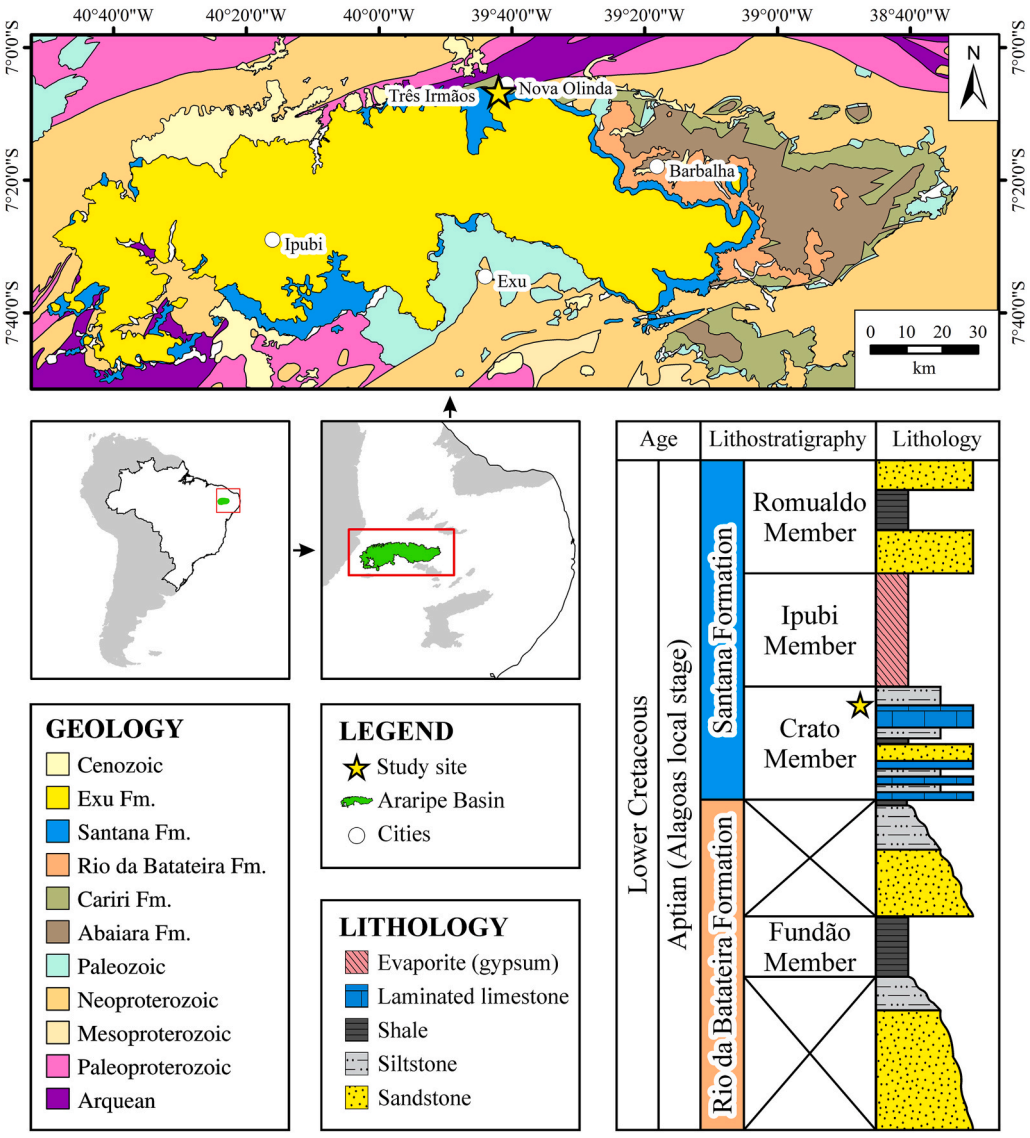

Fig. 1. (Color should be used in this figure) Geological context of the Araripe Basin (Modified from Angelim et al., 2004; Assine, 2007) and simplified stratigraphic profile. The lithostratigraphy was based on Ponte and Appi (1990) and Rios-Netto et al. (2012b), while the chronostratigraphy was obtained from Arai and Assine (2020). The Três Irmãos quarry location (7°6′52.93″S; 39°41′52.45″W) is assigned in the map as a star.

Assine et al., 2014; Neumann, 1999). This geological record is considered one of the most famous fossil *Konservat-Lagerstätten* in the world, where were recognized diversified paleofauna and paleoflora (Martill et al., 2007a; Carvalho et al., 2019; Ribeiro et al., 2021). Furthermore, the member is considered as a key record to understand the opening of the equatorial Atlantic Ocean and, consequently, the evolution of the Pre-Salt Oil Province in the Brazilian Continental Margin Basins.

The Crato Member has been considered as a lacustrine-deltaic depositional system (Neumann, 1999; Heimhofer et al., 2010; Paula--Freitas and Borghi, 2010) and is overlain by gypsum beds of the Ipubi Member, a marine-influenced evaporative-lacustrine depositional system (Lima, 1978; Rios-Netto, 2011; Bobco et al., 2017; Goldberg et al., 2019), and underlain by the Rio da Batateira Formation, a fluvio-lacustrine depositional system (Rios-Netto, 2011; Scherer et al., 2015; Silvestre, 2017). However, marine fossils have been found in the Crato Member, which suggest a marine influence (Barbosa et al., 2004; Goldberg et al., 2019; Varejão et al., 2021a).

Arai (2014) proposed an Aptian Tethyan seaway model involving the Brazilian northeastern sedimentary basins based on paleontological data, being the seaway location one of the most important paleogeographical issues. One model proposed that a connection between the Potiguar and Araripe Basins occurred (Lima, 1978; Dino, 1992), but Assine et al. (2016) showed that a divisor existed between these basins using paleocurrent data and proposed a model linking the Araripe to the Jatobá-Tucano-Recôncavo Basins. However, Tethyan fossils have been systematically found in the Araripe Basin, which weakened the model. The Equatorial Atlantic Ocean opened from west to east, which means that the first marine incursions occurred in the Parnaíba Basin. Another proposition is a connection between the Parnaíba and Araripe Basins (Beurlen, 1971; Arai et al., 1994).

Palynological studies indicate that the Crato Member was deposited during the P-270 biozone (Alagoas local Stage/Aptian) (Regali, 1990; Coimbra et al., 2002; Rios-Netto, 2011; 2012b). However, recent absolute geochronological data indicated a Late Barremian-Early Aptian age to the deposition of Ipubi Member black shales, which suggests a possible Late Barremian age to the Crato Member (Lúcio et al., 2020).

Clay mineralogy and lithogeochemical data have been widely used in paleoenvironmental, paleoclimatic and provenance reconstructions (Chamley, 1989; Weaver, 1989; Meunier, 2005; Craigie, 2018). Teles and Berthou (1995) were the first to study the clay mineralogy of the

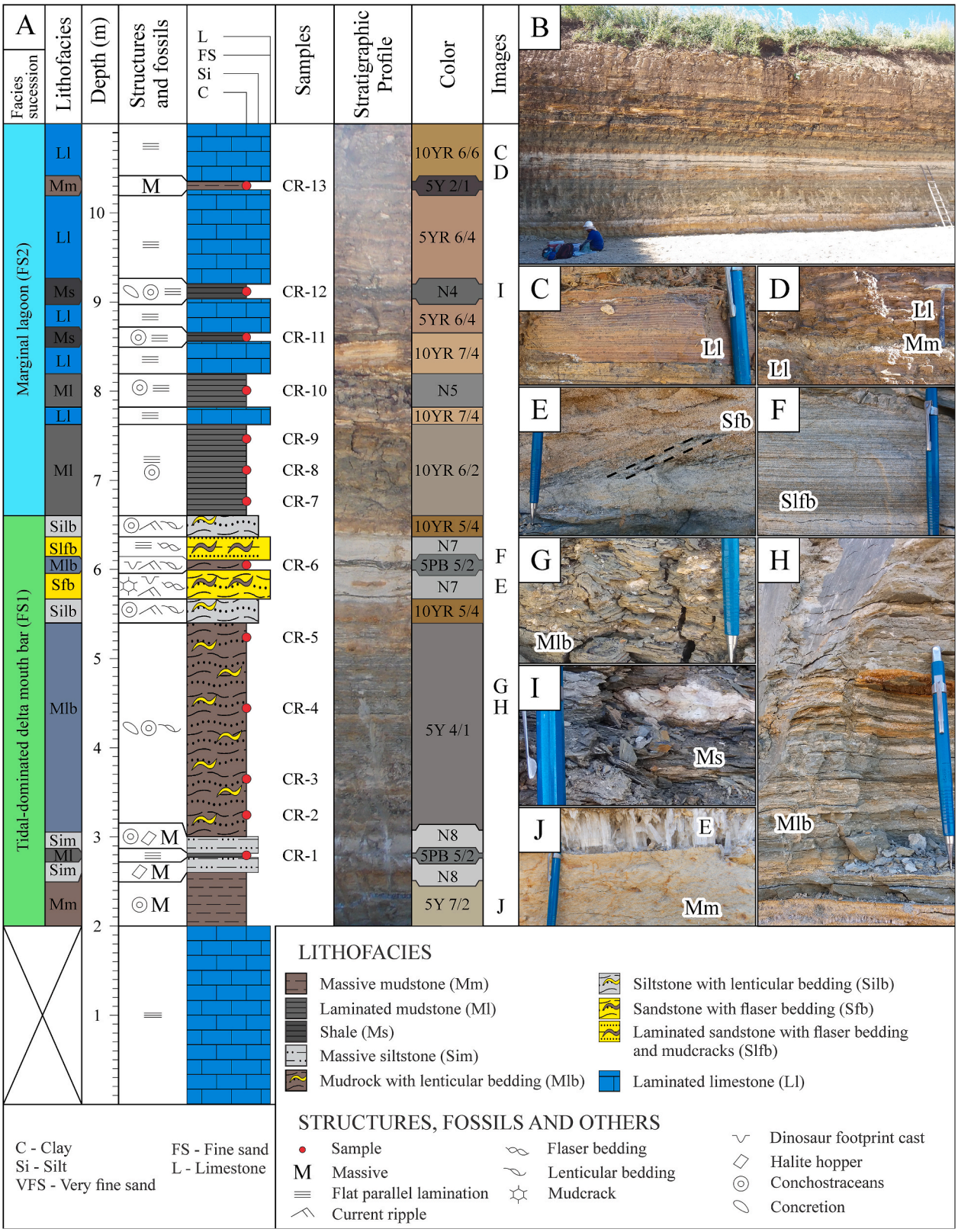

Fig. 2. (Color should be used in this figure) Lithologic profile of the Três Irmãos quarry. A) Lithofacies analysis distributed in facies successions (Symbols from USGS, 2006), sedimentary structures, colors (Munsell, 2009), sampling sites and outcrop image illustrating the whole profile with the location of the following images. B) Três Irmãos quarry overview. C) Laminated limestone (Ll). D) Massive mudstone (Mm) interbedded with laminated limestones (Ll). E) Sandstone with current ripple cross lamination and flaser bedding (Sfb). F) Millimetric alternation of sandstones and shales (Slfb). G, H) Mudstone with lenticular bedding and concretions. I) Shale with the occurrence of manganese minerals. J) Gypsum vein which was considered a secondary feature.

Table 1
Description and interpretation of the lithofacies from the Três Irmãos quarry.

Lithology	Code	Diagnose	Interpretation
Lutites	Ms	Shale	Decantation from suspension in subaqueous environment
	Mm	Massive mudstone	
	Ml	Laminated mudstone	
	Sim	Massive siltstone	
Heterolith	Mlb	Shales with lenticular bedding	Alternation of subaqueous current flow and slack-water conditions with predominance of mud
	Silb	Siltstone with lenticular bedding	
	Sfb	Sandstone with flaser bedding and mudcracks	Alternation of subaqueous current flow and slack-water conditions with predominance of sand with subaereous exposition
	Slfb	Millimetric alternations of laminated sandstones and shales	Tidal rhythmites produced by alternated decantation from suspension of sand/silt and mud in slack-water conditions after hypopycnal flows
Chemical	Ll	Laminated limestone	Biogenic and/or inorganic precipitation of calcium carbonate minerals in low-energy environment

Aptian Formations of the Araripe Basin. Smectite, kaolinite, and illite were identified as the clay mineral assemblage in the Santana and Rio da Batateira Formations, but small contents of chlorite were also found in the last one. The authors attributed the clay mineralogical variations to geomorphological and paleoclimate changes.

Clay mineralogy and lithogeochemistry were not systematically used to study the Crato Member fine-grained rocks, which delayed the real understanding of the geological evolution of these rocks. This study reports the mineralogical and lithogeochemical characterization of the Crato Member lutites aiming at paleoenvironmental, paleoclimatic, and provenance reconstructions.

2. Facies analysis

The study was carried out on an 11-m-thick limestone quarry named Três Irmãos in the Nova Olinda County, Ceará State, which represents nearly 20% of the Crato Member (Figs. 1 and 2). Laminated limestones occur in the base of the section and are lithostratigraphically included in the Martill and Wilby (1993)'s Nova Olinda Member. These rocks represent the above-mentioned fossil *Konservat-Lagerstätten*. Above these rocks occur a 1-m-thick coarsening up succession which appears to be the recently formalized Caldas Bed (Varejão et al., 2021b). The lower siliciclastic part until the top of the second siltstone with lenticular bedding (~6.5 m) and the upper siliciclastic part represents the Martill and Wilby (1993)'s Caldas and Jamacaru Members. Nine lithofacies were determined, being four lutitic, four heterolithic and one chemical (Table 1).

The fine-grained rocks were classified following a modified terminology proposed by Folk (2002), in which shale was used instead of silt-shale, mud-shale and clay-shale. The lutitic lithofacies are composed of decimetric to metric-thick bedset of micaceous massive mudstones (Mm) which occurs twice (Fig. 2D and J), decimetric to metric-thick bedset of micaceous laminated mudstones (Ml) which occurs three times, decimetric-thick bedset of shales with concretions (Ms) which occurs twice (Fig. 2I) and decimetric-thick bedset of micaceous massive siltstones (Sim) which occurs twice.

The heterolytic lithofacies comprises decimetric to metric-thick bedset of micaceous nodular mudstones with lenticular bedding (Mlb) which occurs twice (Fig. 2G and H), decimetric-thick bedset of siltstone with lenticular bedding (Silb) which occurs twice, metric-thick well-sorted and well-rounded sandstone with flaser bedding and mud cracks (Sfb) (Fig. 2E) and decimetric-thick bedset of millimetric alternations of well-sorted and well-rounded laminated sandstones and mudstones (Slfb) (Fig. 2F). Last, the only chemical lithofacies comprises laminated limestones (Ll) (Fig. 2C and D) (q.v., Heimhofer et al., 2010; Catto, 2015; Catto et al., 2016). Gypsum veins were considered as secondary features (Fig. 2J) (Duarte and Borghi, 2018). Halite hoppers were identified in the massive mudstone facies (Sim) and Martill et al. (2007b) studied such structures and identified five different morphologies, in which their type 3 appears to belong to the same stratigraphical level of the occurrences assigned here, being there interpreted as indicative of hypersaline conditions. Dinosaur trampling was recognized in the sandstone with flaser bedding (Slf) and in the mudstone with lenticular bedding lithofacies (Mlb). Those structures were recently better studied by Carvalho et al. (2020) and were interpreted as originated from alkaline lake margins, where freshwater inputs were common. Conchostraceans were also observed (q.v., Carvalho and Viana, 1993).

Table 2
Facies succession of the Três Irmãos quarry.

Facies sucession	Diagnose	Interpretation
Tidal-dominated delta mouth bar (FS1)	Mm/Ml-Sim-Mlb-Silb-Sfb-Mlb-Slfb-Silb	Coarsening-upward profile with deposits originated from hypopycnal flows in a tide-dominated delta mouth bar
Marginal lagoon (FS2)	Successive Ms/Mm-Ll	Marginal lagoon deposits with alternation of mud deposited from decantation originated from hypopycnal overflows and chemical deposition

Two facies successions were interpreted (Table 2), in which the first one (FS1) represents a complete coarsening-upward and shallowing-upward profile of a tidal-dominated delta mouth bar, which was correlated to the Neumann (1999)'s *Associación de facies deltaica*. The second facies succession is composed of successive Ml/Ms-Ll pairs with varying thicknesses and was interpreted as a marginal paleolagoon paleoenvironment, which may be correlated to the Neumann (1999)'s *Associación de facies interna mixta*.

3. Materials and methods

Thirteen lutite samples were collected along the Três Irmãos quarry, being five Ml, one Mm, five Mlb, and two Ms facies (Fig. 2). The samples were dried at 60 °C for 16 h, submitted to ball milling in 106 μm in agate grinding media, and processed in a McCrone mill for 10 min to obtain less than 10 μm bulk samples for semi-quantitative phase analysis, while other less than 106 μm aliquots were submitted to a carbonate removal process (Modified from Carrado et al., 2006; q. v. Coimbra et al., 2021) followed by clay-sized separation (<2 μm) using the Stokes' law for clay mineralogy studies (Moore and Reynolds, 1997).

Semi-quantitative phase analyses (Rietveld) (Cheary and Coelho, 1992; Young, 1993) were carried out in bulk samples (<10 μm) in a Bruker-AXS D4 Endeavor diffractometer, using filtered CoKα radiation ($\lambda = 1.79021$ Å) operating at 40 kV and 40 mA with a step size of 0.01° 2θ and cumulative acquisition time of 184 s/step with a LynxEye position-sensitive detector in the range from 4 to 105° 2θ. A Bruker-AXS TOPAS v5 software was used for the semi-quantitative phase analysis, while the ICDD database (2019) and the Crystallographic Open Database (COD) were used as the source of structures, in which were used structures of montmorillonite (COD 900277; Viani et al., 2002), muscovite (ICDD 04-015-8226; Brigatti et al., 2008), kaolinite (ICDD 00-014-0164 BISH; Goodyear and Duffin, 1961), quartz (ICDD 00-046-1045; Kern and Eysel, 1993), microcline (ICDD 00-019-0926; Technisch Physiscge Dienst, 1966), calcite (Modified; Santos et al., 2017) and dolomite (Modified; Santos et al., 2017). Abbreviations for names of rock-forming minerals were from Whitney and Evans (2010) and Warr (2020).

Samples on oriented glass slides were air-dried, ethylene-glycol solvated for 16 h, and heated at 550 °C for 2 h to determine the clay mineral

Table 3
Classification by Pearson correlation coefficients.

ρ value (+or -)	Interpretation
0.00 to 0.19	Very weak correlation
0.20 to 0.39	Weak correlation
0.40 to 0.69	Moderate correlation
0.70 to 0.89	Strong correlation
0.90 to 1.00	Very strong correlation

groups. Random mounted samples were prepared by backloading to study the clay mineral species through *d*060 analysis (Moore and Reynolds, 1997). The diffraction patterns of the oriented glass slides were obtained with a Bruker-AXS D8 Advance ECO diffractometer with a LynxEye XE energy-discriminant position-sensitive detector using a dynamic beam optimization (DBO) and unfiltered CuKα radiation (λ = 1.5406 Å) operated at 40 kV and 25 mA, 0.01° 2θ step size and cumulative 92 s/step.

The random samples were mounted by backloading and analyzed in a Bruker-AXS D8 Advance ECO equipment, 0.01° 2θ step and cumulative

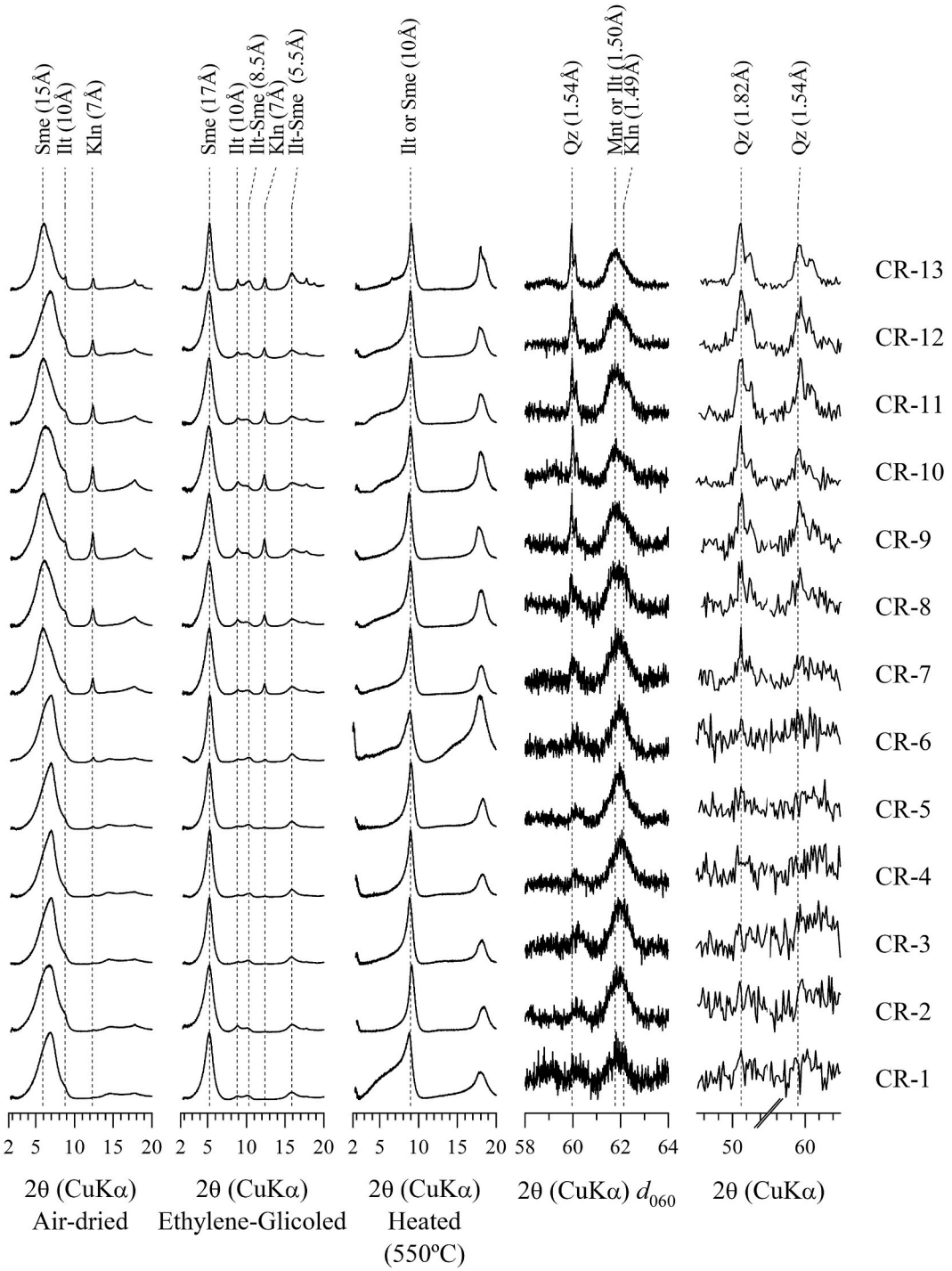

Fig. 3. Background-subtracted and normalized by maximum intensity XRD patterns of the clay-sized fraction of the Crato Member lutites. The unprocessed files can be found in the supplementary files. Sme – Smectite; Ilt – Illite; Kln – Kaolinite; Ilt-Sme - Illite-smectite mixed layered clay minerals; Qz – Quartz; Mnt – Montmorillonite.

Table 4
Semi-quantitative mineral analysis (wt.%) (Biscaye, 1965) and mineralogical features of the clay-sized fraction of the Crato Member lutites. See table S1 in the supplementary files for more details. FWHM – full width at half maximum. Ilt in Ilt-Sme (%) – Illite percentage in illite-smectite mixed layered clay minerals.

Clay mineralogy (%)	CR-1	CR-2	CR-3	CR-4	CR-5	CR-6	CR-7	CR-8	CR-9	CR-10	CR-11	CR-12	CR-13
Montmorillonite	87.4	83.8	84.5	87.8	78.5	79.6	71.8	65.9	56.7	59.3	66.1	75.9	57.6
Illite	10.7	15.2	10.9	8.3	13.1	11.7	11.6	15.4	18.5	18.5	14.5	10.8	20.7
Kaolinite	1.9	1.0	4.6	3.9	8.4	8.7	16.6	18.7	24.8	22.2	19.4	13.3	21.7
Total	100.0	100.0	100.0	100.0	100.0	100.0	100.0	100.0	100.0	100.0	100.0	100.0	100.0
Mineralogical proxies													
Ilt in Ilt-Sme (%)	22	24	21	17	20	21	26	35	36	33	29	26	19
$FWHM_{Sme}$ (2θ)	1.19	1.36	1.01	0.98	1.02	0.93	1.24	1.34	1.34	1.42	1.31	1.32	0.86

184 s/step 58 to 64° 2θ. To determine if reflections at 1.54 Å are associated with trioctahedral clay minerals or quartz, they were compared to reflections at 1.82 Å as suggested by Moore and Reynolds (1997). Random mounted samples were analyzed in the Bruker-AXS D8 Advance ECO diffractometer with a 0.02° 2θ for 92 s/step s in the range from 4 to 70° 2θ. The semi-quantitative clay mineral analysis mineral was performed based on Biscaye (1965). A new illite-kaolinite-montmorillonite ternary graph was produced to paleoclimate reconstructions using the relative proportions between kaolinite and montmorillonite contents and paleoprecipitation rates (Felsic rocks graph; Barshad, 1966), in which 250 mm (69% Montmorillonite; 31% Kaolinite), 400 mm (45% Mnt; 55% Kln), 600 mm (26% Mnt; 74% Kln) and 1000 mm (7% Mnt; 93% Kln) paleoprecipitation values were used.

Whole elemental geochemical analyses were performed in bulk samples by the Act Labs (Code 4LITHO (11+) Major Elements Fusion ICP (WRA)/Trace Elements Fusion ICP/MS(WRA4B2)) (Certificate of analysis may be found in the Supplementary files). A Pearson correlation matrix was produced (Table S3) and the values were classified according to Table 3. To use the A–CN–K (CIA) ternary graph to evaluate paleoweathering settings, the samples must be carbonate-free. Because of it, the chemical contents related to carbonate minerals were removed from the chemical assay before calculation (Table S2).

Scanning electron microscopy was performed in the bulk samples and images of backscattering electrons were acquired in an FEI Quanta 400 microscope operated at 20 kV coupled to a Bruker Nano Quantax 800 energy-dispersive X-ray fluorescence spectrometer (EDS) with XFlash 5010 detector. The samples were sputter-coated with silver in a Bal-Tec SCD 005 equipment for 250 s at 30 mA.

4. Results

4.1. Clay mineralogy

Smectite was identified by reflections at 15 Å, which swelled to 17 Å after ethylene-glycol solvation and reduced to 10 Å after heating at 550 °C (Brindley and Brown, 1980) (Fig. 3). Illite was determined by reflections at 10 Å, which did not suffer swelling after ethylene-glycol solvation and heating at 550 °C. Kaolinite was identified by reflections at 7 Å, which did not change after ethylene-glycol solvation and collapsed after heating at 550 °C. Montmorillonite was determined as the smectite species by reflections at 1.50 Å, which was also associated with illite, while small reflections at 1.49 Å were attributed to kaolinite (Moore and Reynolds, 1997). The semi-quantitative clay mineral analyses are expressed in Table 4.

Illite-smectite mixed layered clay minerals were identified by reflections close to 8.5 and 5.5 Å after ethylene-glycol solvation. A subtle reflection at 14 Å after heating at 550 °C in sample CR-13 was possibly associated with chlorite, but the absence of a reflection at 14 Å after ethylene-glycol solvation hindered its identification.

4.2. Bulk mineralogy

Smectite, mica, and kaolinite were identified by diagnostic reflections at 15, 10, and 7 Å, respectively (Fig. 4). Quartz was identified

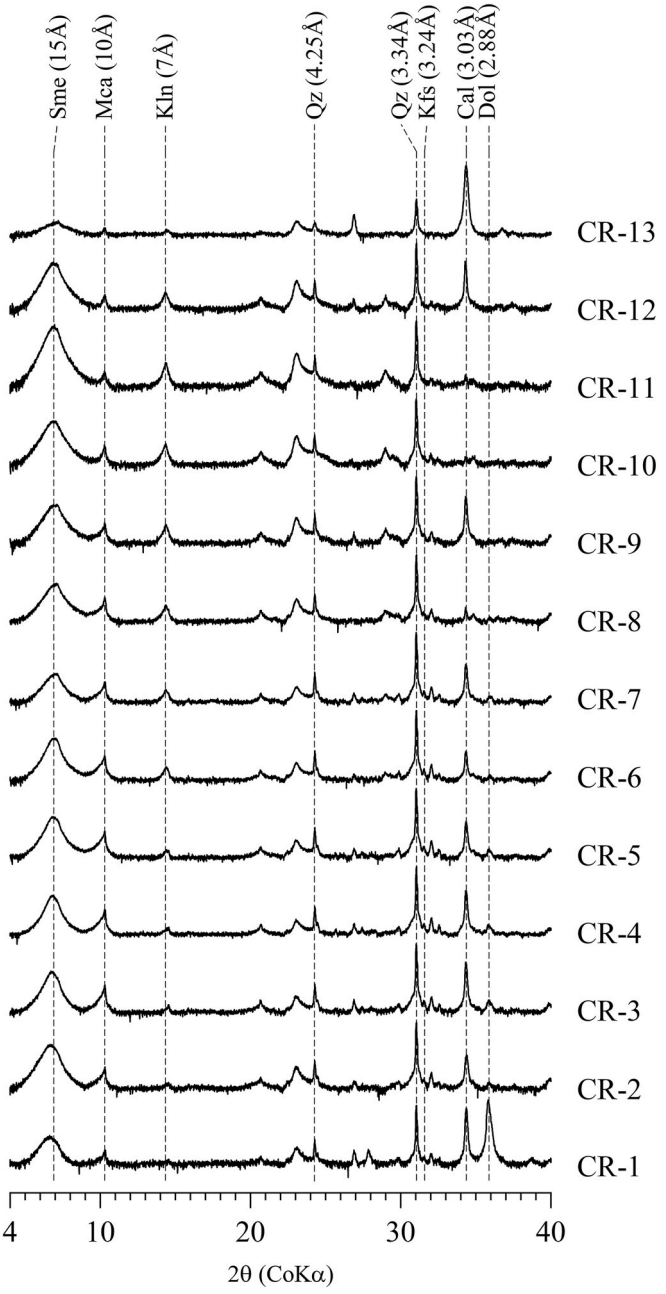

Fig. 4. Background-subtracted and normalized by maximum intensity XRD patterns of the bulk samples of the Crato Member lutites. The y-axis is in the quadratic scale and the unprocessed files can be found in the supplementary files. Sme – Smectite; Mca – Mica; Kln – Kaolinite; Qz – Quartz; Kfs – K-feldspar; Cal – Calcite; Dol – Dolomite.

Table 5
Semi-quantitative phase analysis (wt.%) (XRD/Rietveld) and chemical analyses of major elements (wt.%) of bulk samples of the Crato Member lutites. See table S2 in the supplementary files for more details.

Mineralogy	CR-1	CR-2	CR-3	CR-4	CR-5	CR-6	CR-7	CR-8	CR-9	CR-10	CR-11	CR-12	CR-13
Smectite	15.0	37.5	30.3	29.2	31.8	34.6	22.3	29.6	19.0	32.7	43.2	46.0	7.9
Mica	10.7	16.9	10.6	10.6	12.6	14.1	10.5	19.4	17.8	19.1	21.1	12.0	3.9
Kaolinite	4.4	5.4	5.0	4.2	5.5	11.0	18.5	20.3	26.9	25.0	16.5	13.0	16.4
Quartz	8.9	16.0	19.0	23.7	22.8	19.2	22.2	15.7	12.7	11.6	7.7	11.7	6.7
K-feldspar	7.7	13.9	12.5	11.1	13.3	13.4	11.1	11.3	10.4	9.3	8.5	6.2	1.9
Calcite	18.7	9.4	21.2	20.3	12.9	7.4	14.3	3.2	12.9	2.1	2.5	11.1	63.3
Dolomite	34.5	0.9	1.4	0.9	1.2	0.2	1.0	0.5	0.5	0.3	0.5	0.0	0.0
Total	100.0	100.0	100.0	100.0	100.0	100.0	100.0	100.0	100.0	100.0	100.0	100.0	100.0
Chemical assay													
SiO_2	26.75	47.44	45.07	46.98	49.26	49.84	48.82	49.83	45.30	49.56	49.46	45.53	24.66
Al_2O_3	7.83	14.44	12.89	13.28	14.11	15.27	14.91	18.12	16.96	19.68	19.48	17.16	8.48
Fe_2O_3	5.51	6.28	5.78	4.96	5.26	5.74	5.01	6.32	5.68	6.88	5.31	5.48	3.27
MnO	0.40	0.08	0.12	0.12	0.13	0.08	0.11	0.05	0.08	0.03	0.04	0.07	0.17
MgO	8.05	4.78	4.63	4.22	4.46	4.29	3.58	3.89	3.48	2.81	3.25	3.09	2.59
CaO	19.66	5.01	9.49	9.48	6.55	4.44	7.66	1.81	6.22	1.73	1.97	6.63	26.86
Na_2O	0.12	0.17	0.22	0.33	0.27	0.22	0.25	0.10	0.09	0.14	0.16	0.25	0.54
K_2O	1.60	3.08	3.01	3.08	3.21	3.02	2.94	3.18	2.79	2.73	2.38	2.21	1.08
TiO_2	0.39	0.75	0.67	0.68	0.72	0.80	0.69	0.89	0.71	0.74	0.59	0.51	0.29
P_2O_5	0.12	0.17	0.17	0.16	0.17	0.20	0.28	0.22	0.28	0.16	0.20	0.61	0.47
LOI	29.46	17.97	17.99	17.19	16.44	15.54	16.25	14.41	17.73	16.30	17.84	19.09	32.04
Total	99.89	100.17	100.04	100.48	100.57	99.44	100.49	98.82	99.32	100.76	100.68	100.63	100.45
K_2O/Al_2O_3	0.20	0.21	0.23	0.23	0.23	0.20	0.20	0.18	0.16	0.14	0.12	0.13	0.13
DF1	3.73	4.77	4.31	3.65	3.93	4.22	3.83	5.37	5.17	4.57	3.73	3.02	0.57
DF2	−4.06	−1.46	−1.66	−1.66	−1.90	−1.39	−1.26	−1.36	−1.52	−0.15	−0.92	0.08	−0.65

Table 6
Trace elements (ppm) of the Crato Member lutites.

Elements	CR-1	CR-2	CR-3	CR-4	CR-5	CR-6	CR-7	CR-8	CR-9	CR-10	CR-11	CR-12	CR-13
Sc	7	13	12	12	13	17	14	20	19	20	19	18	8
Be	2	3	2	2	3	3	3	4	3	3	3	3	1
V	77	113	90	78	90	115	95	133	135	156	166	146	143
Ba	261	454	632	610	597	542	543	426	332	298	259	266	179
Sr	207	191	191	188	188	142	197	126	157	90	164	196	555
Y	16	17	18	18	19	21	26	24	23	17	14	19	8
Zr	111	149	110	130	129	178	181	135	113	131	106	93	53
Cr	50	100	90	90	90	130	100	110	100	100	100	90	50
Co	12	18	24	20	15	21	22	25	39	11	25	33	14
Ni	30	50	50	50	40	60	60	70	70	50	40	50	30
Cu	30	40	40	30	30	40	60	80	80	90	90	120	90
Zn	110	160	140	160	190	420	130	140	140	440	1080	1250	1690
Ga	12	23	20	21	22	27	21	27	24	26	25	22	12
Ge	<1	1	1	1	1	1	1	2	1	1	1	1	<1
As	<5	<5	<5	<5	<5	<5	<5	<5	5	11	9	16	8
Rb	71	150	146	147	151	141	135	161	136	128	109	108	50
K	13,282	25,568	24,987	25,568	26,648	25,070	24,406	26,399	23,161	22,663	19,757	18,346	8966
Nb	10	19	16	17	17	18	16	22	17	18	14	12	7
Mo	<2	2	3	2	<2	<2	2	<2	2	2	2	5	3
Ag	<0.5	0.6	<0.5	0.6	0.5	0.6	0.7	0.6	0.5	0.6	0.5	0.6	<0.5
In	<0.2	<0.2	<0.2	<0.2	<0.2	<0.2	<0.2	<0.2	<0.2	<0.2	<0.2	<0.2	<0.2
Sn	6	4	3	3	4	4	3	4	3	3	3	3	2
Sb	<0.5	<0.5	<0.5	<0.5	<0.5	<0.5	<0.5	<0.5	<0.5	<0.5	<0.5	<0.5	<0.5
Cs	2.9	6.5	6.1	5.4	5.9	5.6	5.2	7.4	6.7	6.7	6.4	6.6	3.4
La	33.1	49.1	44.8	50.2	45.8	55.1	43.3	63.3	52.8	38.5	28.7	40.7	18.0
Hf	4.8	4.4	3.8	3.5	3.5	3.4	3.4	3	2.9	2.8	2.8	2.5	1.5
Ta	1.2	1.4	1.4	1.6	1.3	1.3	1.3	0.9	1.2	0.8	1.2	0.9	0.6
W	8	8	6	5	4	13	16	4	3	5	11	10	5
Tl	0.7	0.7	0.8	0.8	0.8	0.8	0.8	0.9	0.7	0.3	0.9	1.2	0.5
Pb	18	12	26	14	20	24	15	18	24	27	28	33	22
Bi	<0.4	<0.4	<0.4	0.4	0.4	<0.4	<0.4	<0.4	0.4	<0.4	<0.4	<0.4	<0.4
Th	14	18.7	19.3	23.4	17.3	14.1	15.2	16.1	16.5	9.4	13	15.5	8.6
U	2.5	2.8	3.2	3.7	3.3	2.6	2.5	2.8	3.3	1.7	2.8	3	2.2
Rb/K	0.0053	0.0059	0.0058	0.0057	0.0057	0.0056	0.0055	0.0061	0.0059	0.0056	0.0055	0.0059	0.0056
La/Th	2.36	2.63	2.32	2.15	2.65	3.91	2.85	3.93	3.20	4.10	2.21	2.63	2.09
Th/Sc	2.00	1.44	1.61	1.95	1.33	0.83	1.09	0.81	0.87	0.47	0.68	0.86	1.08
Th/Co	1.17	1.04	0.80	1.17	1.15	0.67	0.69	0.64	0.42	0.85	0.52	0.47	0.61
Th/Cr	0.28	0.19	0.21	0.26	0.19	0.11	0.15	0.15	0.17	0.09	0.13	0.17	0.17
Zr/Sc	15.86	11.46	9.17	10.83	9.92	10.47	12.93	6.75	5.95	6.55	5.58	5.17	6.63
La/Sc	4.73	3.78	3.73	4.18	3.52	3.24	3.09	3.17	2.78	1.93	1.51	2.26	2.25
U/Th	0.18	0.15	0.17	0.16	0.19	0.18	0.16	0.17	0.20	0.18	0.22	0.19	0.26
V/Cr	1.54	1.13	1.00	0.87	1.00	0.88	0.95	1.21	1.35	1.56	1.66	1.62	2.86
V/Ni	2.57	2.26	1.80	1.56	2.25	1.92	1.58	1.90	1.93	3.12	4.15	2.92	4.77

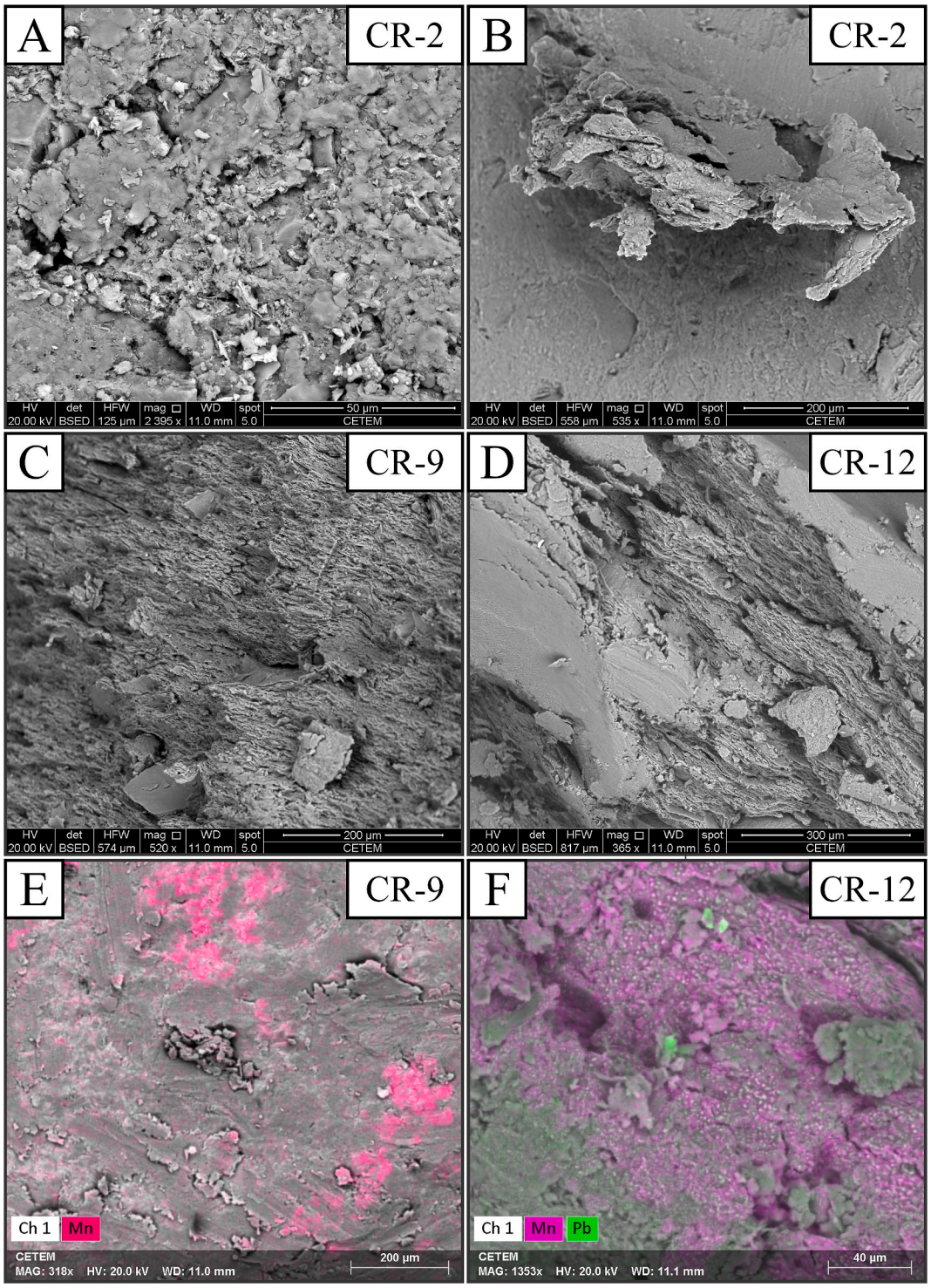

Fig. 5. (Color should be used in this figure) Scanning electron microscopy images of Crato Member lutites. A, B) Detrital montmorillonite and illite in the sample CR-2. C) Detrital montmorillonite, illite and kaolinite in the sample CR-9. D) Detrital montmorillonite, illite and kaolinite in the CR-12 sample. E, F) Compositional maps indicating the distribution of manganese and lead in altered planes.

by reflections at 4.25 and 3.34 Å, whereas K-feldspar was determined at 3.24 Å. Calcite was determined at 3.03 Å and dolomite by the diagnostic reflection at 2.88 Å. The semi-quantitative mineral analyses are expressed in Table 5.

4.3. Scanning electron microscopy

The samples with the highest montmorillonite (CR-2) and kaolinite (CR-9) contents were analyzed by scanning electron microscopy as well as a sample with manganese (Fig. 2I) and base metal anomalies (CR-12) (e.g., Cu and Zn; Table 6). Montmorillonite, illite, and kaolinite were interpreted as detrital because of the platy crystals and absence of honeycomb, rose-shaped, hairy-shaped, and booklets micromorphologies (Fig. 5) (Keller, 1978). Manganese was observed in altered planes associated with lead in the sample CR-12, indicating that the base metal anomalies found in the lithogeochemical analysis from the sample

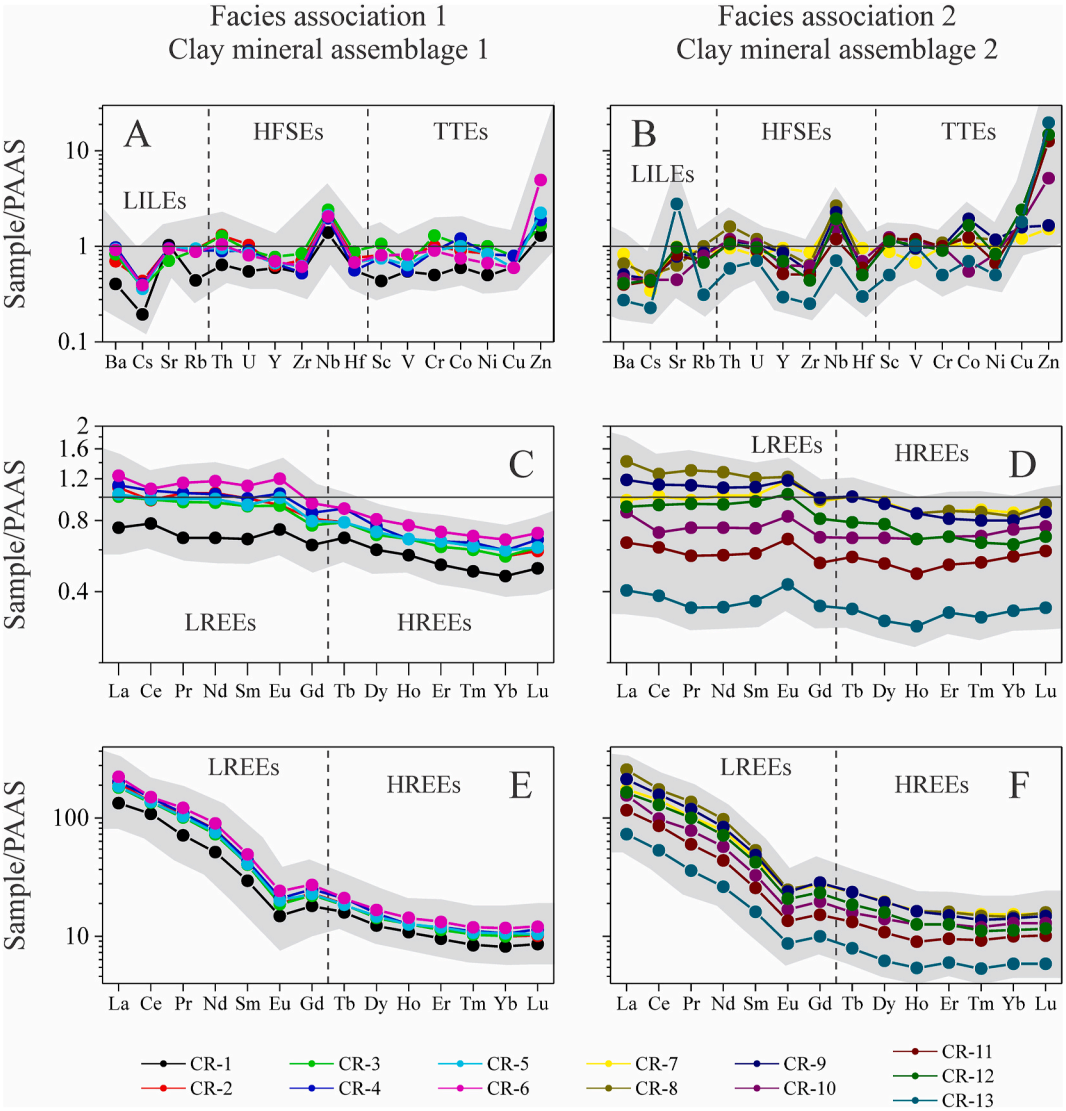

Fig. 6. (Color should be used in this figure) Post-Archean Australian Shale (PAAS) and chondrite normalized trace and rare earth elements spiders of Crato Member lutites. A, B) Trace elements normalized by PAAS values (Taylor and McLennan, 1985; McLennan, 2001). LILE – Large ion lithophile elements. HFSE – High-field strength elements. TTE – Transition trace elements. C, D) Chondrite-normalized REE values (Pourmand et al., 2012). LREE – Light rare earth elements. HREE – Heavy rare earth elements. E, F) PAAS-normalized REE values (Pourmand et al., 2012).

CR-11 to the CR-13 might be associated with the manganese levels (Fig. 5E and F).

4.4. Geochemistry

4.4.1. Major elements

The major element analyses are expressed in Table 5. The samples showed certain homogeneity regarding major elements except for samples CR-1 and CR-13, which are in the downmost and uppermost parts of the profile, respectively. The samples presented K_2O/Al_2O_3 ratios indicating the predominance of illite.

4.4.2. Trace element

Large ion lithophile elements (Ba, Cs, Sr, and Rb)

The trace element distributions are expressed in Table 6. Strong positive correlations were observed between Ba and K_2O (0.80). Strong positive correlations between Cs and SiO_2 (0.86) and Cs and Al_2O_3 (0.89) and strong negative correlations between Cs and CaO (−0.89) and LOI (−0.85) (Table S3). These results indicate that both Ba and Cs are associated with silicate phases (e.g., clay minerals and/or K-feldspar) and that the presence of carbonate phases turn the samples depleted in Ba and Cs in comparison with the Post-Archean Australian Shale (PAAS) (Taylor and McLennan, 1985; McLennan, 2001) (Fig. 6).

A strong positive correlation was observed between Sr and CaO (0.86), Sr and Na_2O (0.85), and Sr and LOI (0.80), and strong negative correlations were observed between Sr and SiO_2 (−0.77), Sr and Fe_2O_3 (−0.88), Sr and K_2O (−0.74), and Sr and TiO_2 (−0.75). These results suggest that Sr is mostly incorporated in carbonate phases (e.g., calcite and dolomite). Almost all samples are depleted in Sr except CR-1 and CR-13 samples, which showed the higher contents of carbonate phases.

Almost all the samples were depleted in Rb in comparison with PAAS. Very strong positive correlations between Rb and K_2O (0.99) and Rb and TiO_2 (0.94), strong positive correlations between Rb and SiO_2 (0.87), and strong negative correlations with CaO (−0.79) were identified, indicating that Rb is also associated with silicate phases.

High-field strength elements (Th, U, Y, Zr, Nb, and Hf)

Table 7
Rare earth elements (ppm) of the Crato Member lutites.

Elements	CR-1	CR-2	CR-3	CR-4	CR-5	CR-6	CR-7	CR-8	CR-9	CR-10	CR-11	CR-12	CR-13
La	33.1	49.1	44.8	50.2	45.8	55.1	43.3	63.3	52.8	38.5	28.7	40.7	18
Ce	68.5	85.8	86.1	94.4	86.8	95.7	89.6	111.0	100.0	62.8	54.3	81.9	33.9
Pr	6.83	10.60	9.70	10.60	10.00	11.70	9.86	13.20	11.40	7.57	5.75	9.56	3.46
Nd	25.1	38.9	35.4	38.4	36.8	43.6	38.1	47.7	40.9	27.7	21.3	34.9	12.8
Sm	4.6	6.8	6.3	6.8	6.4	7.7	7.0	8.3	7.6	5.1	4.0	6.6	2.5
Eu	0.89	1.13	1.12	1.26	1.21	1.46	1.43	1.48	1.43	1.01	0.81	1.25	0.52
Gd	3.8	4.9	4.6	5.2	4.8	5.7	5.8	5.9	6	4.1	3.2	4.9	2.1
Tb	0.6	0.7	0.7	0.8	0.7	0.8	0.9	0.9	0.9	0.6	0.5	0.7	0.3
Dy	3.2	3.7	3.7	4.0	3.8	4.3	5.1	5.0	5.0	3.6	2.8	4.1	1.6
Ho	0.6	0.7	0.7	0.7	0.7	0.8	0.9	0.9	0.9	0.7	0.5	0.7	0.3
Er	1.6	1.9	1.9	2.0	2.0	2.2	2.7	2.7	2.5	2.1	1.6	2.1	1.0
Tm	0.22	0.27	0.27	0.29	0.28	0.31	0.40	0.39	0.36	0.31	0.24	0.29	0.14
Yb	1.4	1.7	1.7	1.8	1.8	2.0	2.6	2.5	2.4	2.2	1.7	1.9	1.0
Lu	0.22	0.26	0.27	0.29	0.27	0.31	0.40	0.41	0.38	0.33	0.26	0.30	0.15
LREE	139.0	192.3	183.4	201.7	187.0	215.3	189.3	245.0	214.1	142.7	125.7	189.9	77.8
HREE	17.1	22.1	21.3	23.1	22.0	25.6	27.2	28.5	27.5	20.1	15.6	22.8	9.6
ΣREE	150.7	206.5	197.3	216.7	201.4	231.7	208.1	263.7	232.6	156.6	125.7	189.9	77.8
Eu/Eu^*_{CN}	0.65	0.60	0.64	0.65	0.67	0.67	0.69	0.65	0.65	0.67	0.69	0.67	0.69
Gd_{CN}/Yb_{CN}	2.20	2.34	2.19	2.34	2.16	2.31	1.81	1.91	2.03	1.51	1.53	2.09	1.70
$(La/Yb)_{CN}$	10.80	13.19	12.03	12.74	11.62	12.58	7.60	11.56	10.05	7.99	7.71	9.78	8.22

The samples showed similar values of Th, U and Y in comparison with PAAS. There are no correlations between Th and U and the major elements. Strong positive correlations were observed between Y and K_2O (0.71), Y and TiO_2 (0.72), and Y and TiO_2 (0.72), indicating that the element is mainly controlled by silicate phases. Zr is slightly depleted in comparison with PAAS as well as Hf. Strong positive correlations were observed between Zr and K_2O (0.73) and Zr and TiO_2 (0.74), indicating that the element is also associated with silicate phases.

Nb has very strong positive correlations with K_2O (0.93) and TiO_2 (0.99), strong positive correlations with SiO_2 (0.83) and Fe_2O_3 (0.73), and strong negative correlations with CaO (−0.83) and LOI (−0.88), indicating that the element is controlled by silicate phases. The samples are enriched in Nb in comparison with PAAS.

Transition trace elements (Sc, V, Cr, Co, Ni, Cu, and Zn)

The samples presented TTEs values close to those from PAAS, except for Cu and Zn. There were identified positive anomalies of these elements in all samples, but impressive anomalies were found in samples CR-11, CR-12, and CR-13 with values from 10 to 20 times higher than those expressed in PAAS. These values may be explained by mafic provenance sources or even by hydrothermalism since studies were carried out in the Fundão Member (Rios-Netto et al., 2012a) of the Rio da Batateira Formation aiming at the exploration of base metals (e.g., Cu, Zn and Pb) in a project named Santana during the '70s. Further studies should be carried out to understand the origin of these anomalies.

Rare earth elements

The REE distribution is expressed in Table 7 and is similar in comparison with PAAS, but enriched in LREEs and depleted in HREEs, being the REE quantity controlled mainly by the dilution effect caused by carbonate phases (e.g., calcite or dolomite) (Tobia and Mustafa, 2016), which is corroborated by a moderate negative correlation between ΣREE and CaO (−0.61), and ΣREE and LOI (−0.75) (Table S3). The strong positive correlations between ΣREE and K_2O (0.83) and TiO_2 (0.83) indicate that the REEs are associated with silicate phases. In comparison with chondrite, the samples are enriched in LREEs and depleted in HREEs, which is demonstrated by $(La/Yb)_{CN}$ values ranging from 7.60 (CR-7) and 13.19 (CR-2) (Table 7). The samples showed weak negative anomalies of $(Eu/Eu^*)_{CN}$ from 0.60 (CR-2) to 0.69.

5. Discussions

5.1. Mineralogical and lithogeochemical proxies

Two clay mineral assemblages (CMA) were identified based on semi-quantitative clay mineral analysis. The clay mineral assemblage 1, which is coincident with the tidal-dominated delta mouth bar facies association (FS1), contains lesser kaolinite contents (up to 8.7%) (Fig. 7), whereas the clay mineral assemblage 2, which is coincident with the marginal paleolagoon facies association (FS2), is composed of higher kaolinite contents between 13.3 and 24.8%.

Kaolinite is commonly formed in more wet paleoclimates, where more acid soils develop because of higher paleoprecipitation rates, while smectite is usually formed in more dry paleoclimates, where basic soils develop because of lower paleoprecipitation rates (Barshad, 1966; Singer, 1984; Thiry, 2000; Meunier, 2005; Coimbra et al., 2021). Therefore, the relative proportion of detrital kaolinite and montmorillonite can be used as a paleoprecipitation indicator and, consequently, help in paleoclimatic reconstructions (e.g., Rego et al., 2018; Holanda et al., 2019). Illite contents should not be used as paleoprecipitation proxies because it is directly associated with the mineralogy of the source-rocks (Barshad, 1966).

The relative proportions of kaolinite in respect to montmorillonite indicated low paleoprecipitation values (<250 mm), which is consistent with previous studies that indicated arid paleoclimate conditions in the Equatorial Atlantic Ocean during the Aptian (Petri, 1983; Lima, 1983). Furthermore, these interpretations also corroborate the Boucot et al. (2013)'s Early Cretaceous paleoclimatic map, which defined an arid zone in the Equatorial Atlantic Ocean, and the Chumakov et al. (1995)'s evaporative zone in the Tropical-Equatorial Hot arid belt (Hay and Floegel, 2012).

Nevertheless, a subtle increase in the paleoprecipitation values was observed from the CMA1 to the CMA2, indicating more wet conditions and an intensification of the hydrological cycle in the FS2 (Fig. 8). This humidification might be associated with higher ocean proximity since one of the main causes of the Gondwana aridity during the Aptian probably was the supercontinent effect (Hay and Floegel, 2012), in which the distance between land and sea hindered moisture to enter the continent. Previous studies on clay minerals indicated that low paleoprecipitation conditions occurred not only during the deposition of the Crato Member lutites but also in the Santana as a whole and the Rio da Batateira Formations (Teles and Berthou, 1995).

The Chemical Index of Alteration (CIA) is used to evaluate the paleoweathering conditions that rocks in source areas were submitted

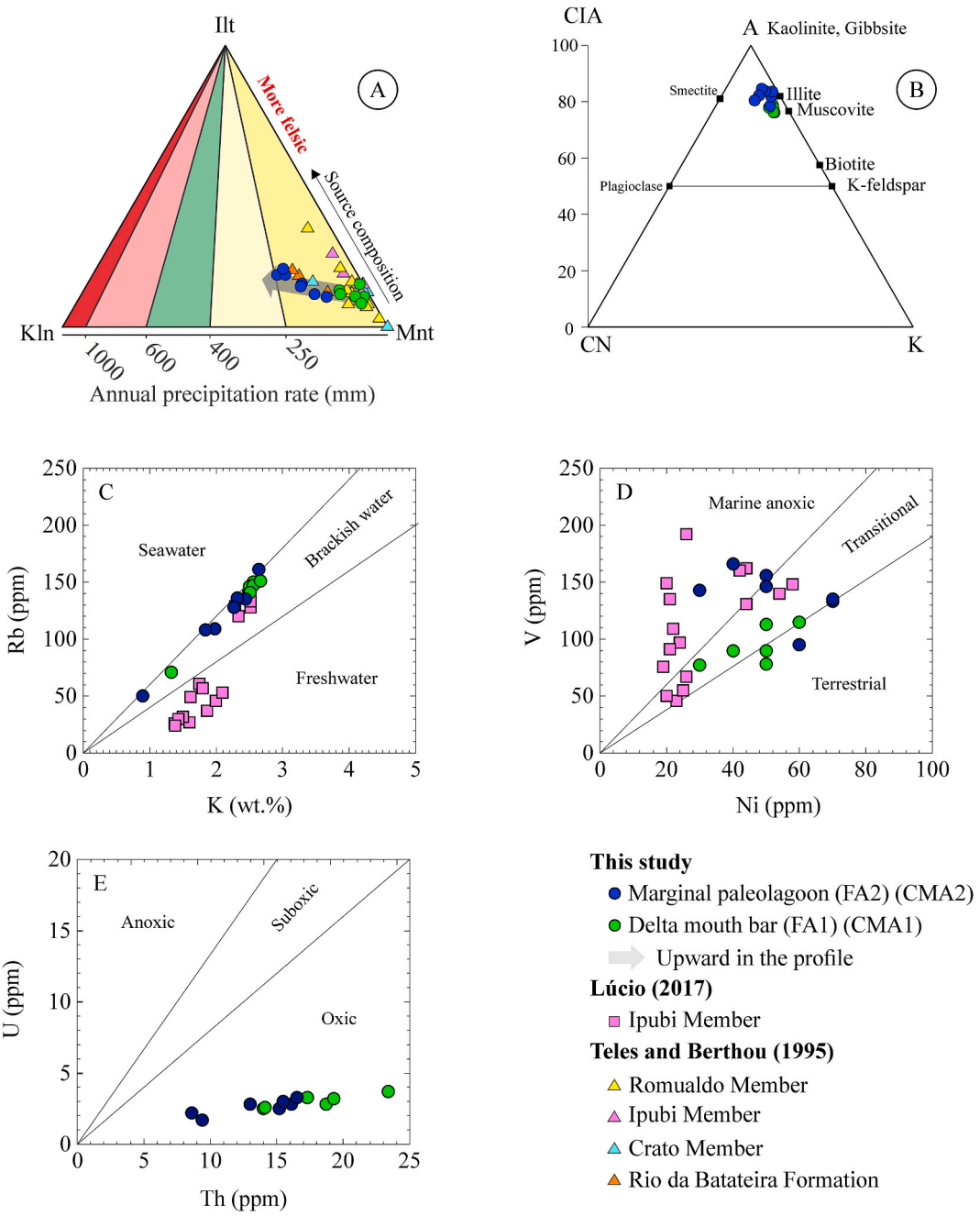

Fig. 7. (Color should be used in this figure) Paleoenvironmental and paleoclimatic proxies of the Crato Member lutites based on clay mineralogy and lithogeochemical data. A) Ternary graph with the relative proportion of smectite, illite and kaolinite obtained from the semi-quantitative mineral analysis (Biscaye, 1965) using the relative proportions between kaolinite and montmorillonite from Barshad (1966) to indicate paleoprecipitation values. B) A–CN–K (CIA) ternary diagram (Nesbitt and Young, 1984). See table S1 in the supplementary files to see how the data used in this graph was calculated. C) Rb (ppm) versus K (wt.%) graph (Campbell and Lerbekmo, 1963; Campbell and Williams, 1965; Visser and Young, 1990; Geiger, 2010). D) V (ppm) versus Ni (ppm) graph (Galarraga et al., 2008). E) U (ppm) versus Th (ppm) graph (Adams and Weaver, 1958; Jones and Manning, 1994; McKirdy et al., 2011; Sari and Koca, 2012).

based on major elements (Nesbitt and Young, 1984). The FS1 samples presented CIA values ranging from 76.12 to 78.86, whereas the CMA2 samples presented higher CIA values varying from 78.52 to 84.56, indicating that the source area in the CMA2 was submitted to a more intense paleoweathering than the CMA1 (Figs. 7B and 8D), which is corroborated by the paleoclimate interpretations using clay mineralogy.

A paleosalinity proxy based on Rb/K ratios was determined by the correlative behavior between lutites deposited in marine and non-marine settings (Campbell and Lerbekmo, 1963; Campbell and Williams, 1965; Visser and Young, 1990; Geiger, 2010). The samples plotted in the brackish water field in the Rb versus K bivariate graph, but some FS2 samples plotted close to the seawater field (Figs. 7C and 8E).

Three trends of paleosalinity decreasing were observed and can be associated with the intensification of the hydrological cycle above-mentioned. Three sudden paleosalinity increasing events were identified and were interpreted as seawater inputs, indicating a marine influence, which is corroborated by marine paleofauna occurrences in the Crato Member (Barbosa et al., 2004; Goldberg et al., 2019; Varejão et al., 2021a).

Geochemical data provided by Lucio (2017) indicated that the Ipubi Member black shales were deposited in fresh or brackish water settings, indicating stratification in the paleolagoon water, which corroborates

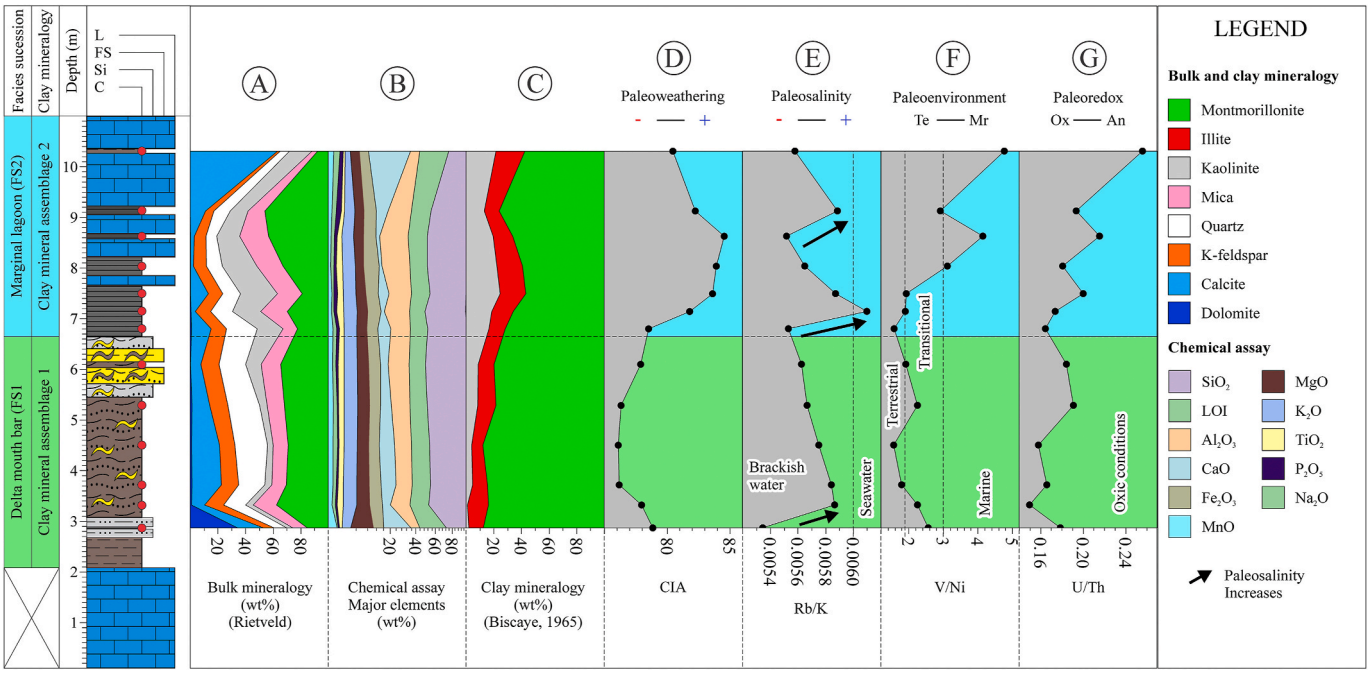

Fig. 8. (2-column landscape figure) (Color should be used in this figure) Paleoenvironmental and paleoclimatic proxies of the Crato Member lutites based on clay mineralogy and lithogeochemical data. See facies description in Table 1. A) Bulk mineralogy (wt.%) of lutites from the Três Irmãos quarry. B) Chemical assay of major elements (wt.%) of lutite from the Três Irmãos quarry. C) Clay mineralogy of lutites from the Três Irmãos quarry. D) Paleoweathering proxy based on A–CN–K (CIA) ternary graph (Nesbitt and Young, 1984). See table S1 in the supplementary files to see how the data used in this graph was calculated. E) Paleosalinity proxy based on Rb/K ratio (Campbell and Lerbekmo, 1963; Campbell and Williams, 1965; Visser and Young, 1990; Geiger, 2010). F) Paleoenvironmental proxy based on V/Ni ratios (Galarraga et al., 2008). G) Paleoredox proxy based on U/Th ratios (Adams and Weaver, 1958; Jones and Manning, 1994; McKirdy et al., 2011; Sari and Koca, 2012).

the Neumann and Cabrera (2002)'s model. Storari et al. (2021) recently reported mayflies' mass mortality events in the Crato Member laminated limestones, which were interpreted as being caused by increases of salinity due to paleolake contractions. However, the seawater inputs interpreted herein may be an alternative explanation for these events.

Galarraga et al. (2008) correlated vanadium and nickel values of nonmature crude oil samples to paleoenvironment settings and developed a method to use these trace elements as paleoenvironmental proxies. Adegoke et al. (2014) demonstrated the applicability of this method to siliciclastic fine-grained rocks. The FS1 samples presented V/Ni ratios plotted mostly in the terrestrial to transitional fields, whereas the FS2 samples plotted indicating a wide distribution in the terrestrial, but mostly in the transitional to marine anoxic fields (Fig. 7D). Such results indicate that the organic matter of the Crato Member lutites is mostly derived from a mixed marine-terrigenous origin, but more marine in the FS2 (Fig. 8F). Otherwise, Lucio (2017) indicates that the organic matter of the Ipubi Member black shales is mostly derived from marine settings, suggesting that the paleoenvironmental settings changed from terrestrial to marine anoxic conditions from the Crato to the Ipubi Member. The trend to marine is corroborated by the strong positive correlation between V/Ni and elevation (0.64).

Paleoredox reconstructions can be made using U/Th ratios (Adams and Weaver, 1958; Jones and Manning, 1994; McKirdy et al., 2011; Sari and Koca, 2012). The FS1 samples presented U/Th values indicating oxic conditions (Fig. 7E). However, a subtle trend to dysoxic conditions was observed (Fig. 8G), which is corroborated by the strong positive correlation between elevation and U/Th (0.71).

5.2. Composition and tectonic settings of source rocks

Elemental geochemical data has been used to reconstruct the composition and tectonic settings of source rocks. In elemental ratios, the numerator field is filled with an incompatible element, while a compatible element fills the denominator. Because of it, the higher is the ratio, the more evolved and felsic is the source rock (Taylor and McLennan, 1985).

Table 8
Elemental ratios of the Crato Member lutites and comparisons with felsic and mafic sources. The first and second numbers represent the minimum and maximum values, respectively, while the value in parenthesis is the average.

Elemental ratio	Delta mouth bar (FS1) (CMA1)	Marginal lagoon (FS2) (CMA2)	Felsic rocks	Mafic rocks
Th/Sc	0.83–2.00 (1.46)	0.47–1.08 (0.79)	0.84–20.50	0.05–0.22
Th/Co	0.67–1.17 (0.96)	0.42–0.85 (0.59)	0.67–19.40	0.04–1.40
Th/Cr	0.11–0.28 (0.20)	0.09–0.17 (0.15)	0.13–2.70	0.018–0.046
La/Sc	3.09–4.73 (3.75)	1.51–3.17 (2.32)	2.50–16.30	0.43–0.86
Eu/Eu*	0.60–0.67 (0.65)	0.65–0.69 (0.68)	0.40–0.94	0.71–0.95

Elemental ratios as well as Eu anomalies of the Crato Member lutites indicated provenance from felsic rocks (Table 8). However, the FS1 samples presented trace element ratios indicating less evolved rocks as a sediment source than the FS2 samples. The samples plotted in the acid and/or intermediate composition field in the K versus Rb diagram (Fig. 9A) (Floyd and Leveridge, 1987) except for the CR-13 sample, which plotted in the basic composition field. The FS1 samples plotted in the granodiorite to granite source fields in the Th/Sc versus Zr/Sc diagram (Condie, 1993; McLennan et al., 1993), while the FS2 samples indicate andesitic to a felsic volcanic source (Fig. 9B). The FS1 samples plotted close to the andesite composition field in the Th/Co versus La/Sc diagram (Fig. 9C) (Cullers, 2002), whereas the FS2 samples showed more basaltic source compositions. The FS1 and FS2 samples plotted in the fields close to granitic and granodioritic-tonalite fields in the Th/Sc

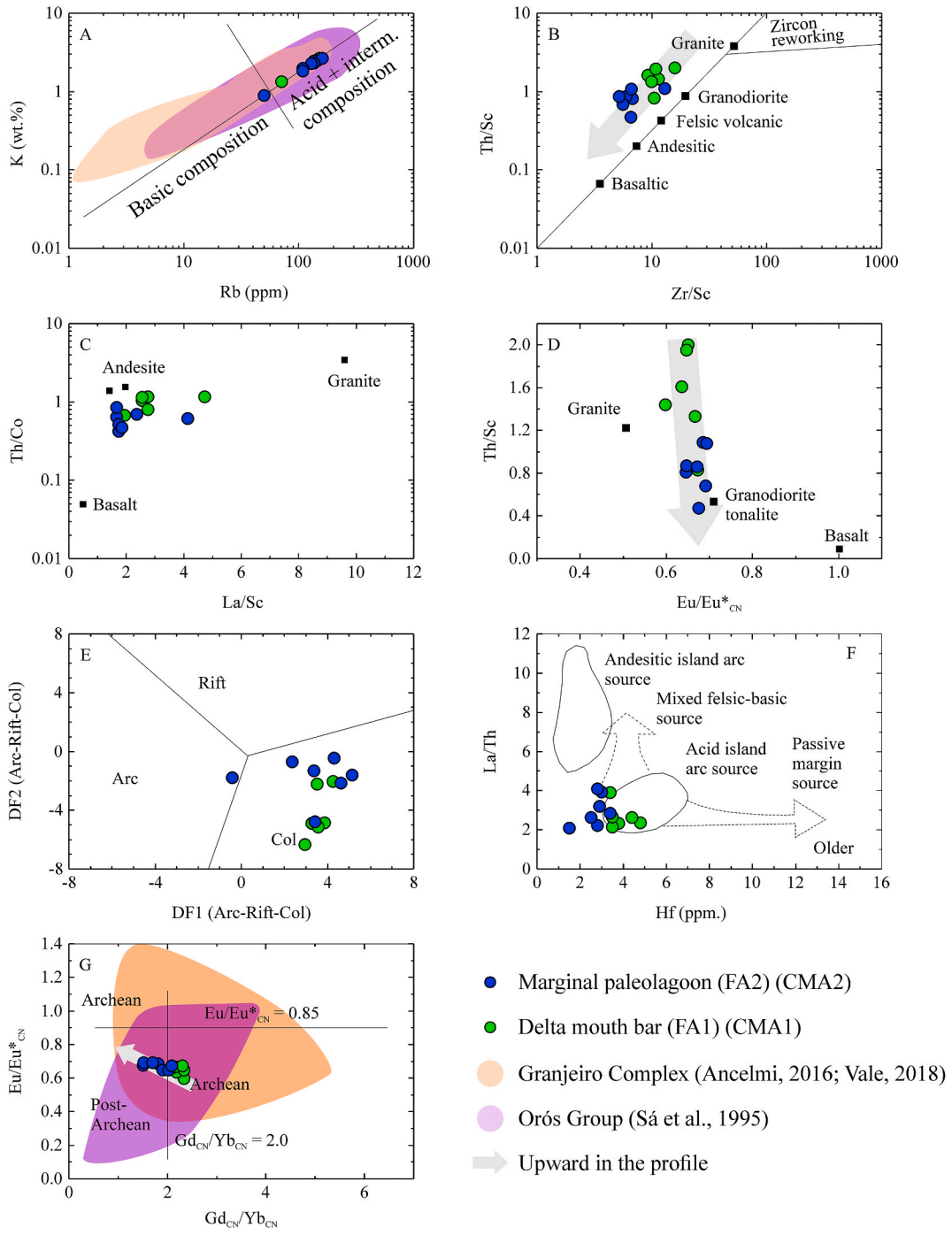

Fig. 9. (Color should be used in this figure) Geochemical diagrams indicating the source composition and tectonic settings of lutites from the Três Irmãos quarry. A) K (wt.%) versus Rb (ppm) diagram (Floyd and Leveridge, 1987). B) Th/Sc versus Zr/Sc diagram (Condie, 1993; McLennan et al., 1993). C) Th/Co versus La/Sc diagram (Cullers, 2002). D) Th/Sc versus Eu/Eu* diagram (Cullers and Podkovyrov, 2002). E) Low-SiO_2 DF2 (Arc-Rift-Col) versus DF1 (Arc-Rift-Col) diagram (Verma and Armstrong-Altrin, 2013). F) La/Th versus Hf diagram (Floyd and Leveridge, 1987). G) Eu/Eu* versus Gd_{CN}/Yb_{CN} diagram (McLennan and Taylor, 1991). Fields were produced in the K (wt.%) versus Rb (ppm) and Eu/Eu* versus Gd_{CN}/Yb_{CN} diagrams using lithogeochemical data from the literature (Sá et al., 1995; Ancelmi, 2016; Vale, 2018).

versus Eu/Eu* diagram (Cullers and Podkovyrov, 2002), respectively (Fig. 9D).

The samples plotted mostly in the collisional field in the low-SiO_2 DF2 versus DF1 diagram (Verma and Armstrong-Altrin, 2013) (Fig. 9E) and mostly in the acid island arc source in the La/Th versus Hf bivariate plot (Floyd and Leveridge, 1987) (Fig. 9F). The FS1 samples plotted in the Archean field, while the FS2 samples plotted in the Post-Archean field in the Eu/Eu* versus Gd_{CN}/Yb_{CN} diagram (McLennan and Taylor, 1991), indicating an age constrain between the source areas (Fig. 9G).

A very strong negative correlation between elevation and La/Sc (−0.90), strong negative correlations between elevation and Th/Sc (−0.78), Th/Co (−0.77) and Zr/Sc (−0.78), and a strong positive correlation between elevation and Eu/Eu^*_{CN} (0.73) were observed (Table S3). These data suggest that despite the provenance of the lutites are associated with intermediate and felsic rocks, there is a trend of increase in the provenance from intermediate rocks upward in the

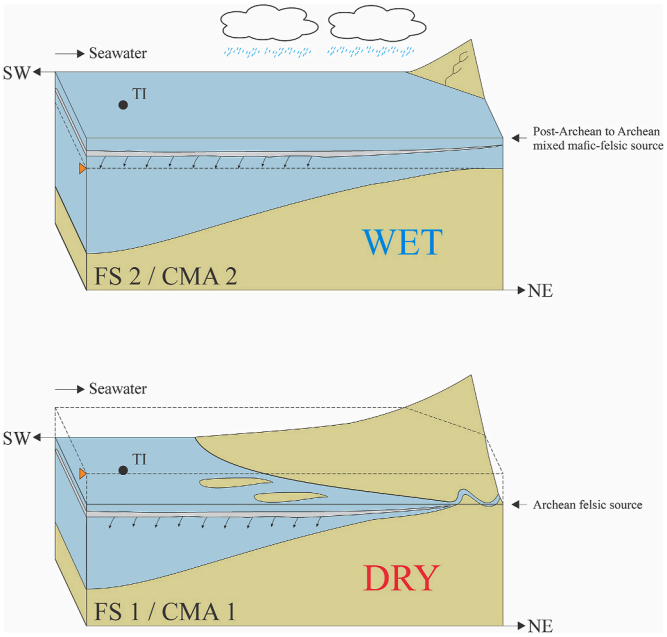

Fig. 10. (Color should be used in this figure) Paleoenvironmental, paleoclimatic and provenance models for the deposition of the Crato Member lutites, indicating the tidal-dominated delta mouth bar facies succession with drier conditions and the marginal paleolagoon facies succession with wetter conditions.

profile.

5.3. *Paleoenvironmental, paleoclimatic and provenance models*

Two paleoenvironmental models were interpreted (Fig. 10). The tidal-dominated delta mouth bar facies succession (FS1) is coincident with the clay mineral assemblage with lesser kaolinite contents, while the marginal paleolagoon facies succession (FS2) is coincident with the clay mineral assemblage with the higher kaolinite contents. Drier conditions took place during the deposition of the first succession, which resulted in weaker paleoweathering settings favoring the formation of smectite instead of kaolinite. Shallow water conditions were observed, as indicated by oxic paleoredox conditions. Concerning the second succession, wetter conditions with higher annual precipitation rates developed, in which stronger paleoweathering conditions developed favoring the formation of kaolinite in soils. Water level deepening occurred, indicated by lesser oxic paleoredox conditions.

The paleolagoon water was interpreted as brackish and cycles of paleosalinity decrease were observed in response to the intensification of the hydrological cycle, but sudden paleosalinity increases indicated seawater inputs, which were also responsible for raising the water table of the paleolagoon in the FS2, which presented paleoenvironmental proxies suggesting marine influence.

Geochemical data indicated that the sediment provenance of the tidal-dominated delta mouth bar facies succession (FS1) came from Archean felsic rocks. This information fits with geological observations since the nearest Precambrian rock association to the Três Irmãos quarry is the Granjeiro Complex, an Archean tonalitic to granodioritic banded gneiss complex with mafic rock occurrences (Silva et al., 1997; Ancelmi, 2016; Vale, 2018) (Fig. 9). As a result of the intensification of the hydrological cycle in the marginal paleolagoon facies succession (FS2), a wider area would be drained, resulting in a Post-Archean to Archean mixed felsic-basic source area. The mixed felsic-mafic Paleoproterozoic volcano-metasedimentary rocks from the Orós Group also may become the source area to the upper Três Irmãos quarry (Sá et al., 1995). Lithogeochemical data of possible source rocks are not easy to find in the literature, which hindered this type of interpretation. However, isotopic geochemical data is quite abundant in literature, and studies using the technique should be made to improve provenance reconstructions.

6. Conclusions

The Crato Member lutites are composed of montmorillonite, kaolinite, and illite as the clay mineral assemblage, being the non-clay minerals mica, quartz, K-feldspar, calcite, and dolomite. This lithostratigraphic unit was considered as a marine-influenced depositional system because of sudden paleosalinity increases and previous marine paleofauna occurrences.

Regional arid paleoclimate conditions were interpreted using clay mineralogy data in the Equatorial Atlantic Ocean during the Aptian. Two paleoenvironmental models with paleoprecipitation and provenance differences were interpreted. A tidal-dominated delta mouth bar facies succession coincident with the clay mineral association with lesser kaolinite content was identified in the lower Três Irmãos quarry, being it deposited in drier conditions and with provenance from Archean felsic rocks.

A marginal paleolagoon facies succession coincident with the clay mineral association with higher kaolinite contents was recognized in the upper Três Irmãos quarry, being this part deposited in wetter conditions and with provenance from Post-Archean to Archean mixed felsic-mafic rocks. Sudden paleosalinity increases indicate seawater inputs into the paleolagoon and were responsible for the deepening of the basin from the tidal-dominated delta mouth bar to the marginal paleolagoon facies succession.

Author statement

Victor Matheus Joaquim Salgado-Campos: Conceptualization, Methodology, Validation, Investigation, Writing - Original Draft, Visualization. **Ismar de Souza Carvalho**: Conceptualization, Investigation, Resources, Writing - Review & Editing, Supervision, Funding acquisition. **Luiz Carlos Bertolino**: Conceptualization, Resources, Writing - Review & Editing, Supervision, Funding acquisition. **Thamiris Agatha Duarte**: Methodology, Validation. **Bruno Cesar Araújo**: Conceptualization, Investigation, Writing - Review & Editing. **Leonardo Borghi**: Conceptualization, Investigation, Supervision, Project administration, Funding acquisition.

Declaration of competing interest

The authors declare that they have no known competing financial interests or personal relationships that could have appeared to influence the work reported in this paper.

Acknowledgements

The authors would like to thank Shell Brasil Petróleo Ltda. For the ongoing R&D project registered as ANP 20.219–2, “Alagoas Project - Stratigraphic correlation, paleo-environmental and paleogeographic evolution and exploratory perspectives of Alagoas Stage” (UFRJ/Shell Brasil/ANP) – ANP (Projeto Alagoas - Correlação estratigráfica, evolução paleoambiental e paleogeográfica e perspectivas exploratória do Andar Alagoas) under the ANP R&D levy as “Compromisso de Investimentos com Pesquisa e Desenvolvimento”. The authors also acknowledge the Centro de Tecnologia Mineral, the Programa de Pós-graduação of the Universidade Federal do Rio de Janeiro (UFRJ), the Laboratório de Geologia Sedimentar of the Universidade Federal do Rio de Janeiro and Aristóteles de Moraes Rios-Netto. Financial support was also received from the Conselho Nacional de Desenvolvimento Científico e Tecnológico (Brazil) (303596/2016-3) and Fundação Carlos Chagas Filho de Amparo à Pesquisa do Estado do Rio de Janeiro (E-26/202.910/2017).

Appendix A. Supplementary data

Supplementary data to this article can be found online at https://doi.org/10.1016/j.jsames.2021.103329.

References

Adams, J.A., Weaver, C.E., 1958. Thorium-to-uranium ratios as indicators of sedimentary processes: example of concept of geochemical facies. AAPG (Am. Assoc. Pet. Geol.) Bull. 42 (2), 387–430.

Adegoke, A.K., Abdullah, W.H., Hakimi, M.H., Yandoka, B.M.S., Mustapha, K.A., Aturamu, A.O., 2014. Trace elements geochemistry of kerogen in Upper Cretaceous sediments, Chad (Bornu) Basin, northeastern Nigeria: origin and paleo-redox conditions. J. Afr. Earth Sci. 100, 675–683.

Ancelmi, M.F., 2016. Geocronologia e geoquímica das rochas arqueanas do Complexo Granjeiro, Província Borborema. Ph.D. thesis Univ. Estad. Camp.

Angelim, L.A.A., Vasconcelos, A.M., Gomes, J.R.C., Wanderley, A.A., Forgiarini, L.L., Medeiros, M.D.F., 2004. Folha SB-24-Jaguaribe. Carta geológica do Brasil ao milionésimo, SIG. Programa geologia do Brasil. CPRM, Brasília. CD-ROM, scale 1.

Arai, M., Lana, C.C., Pedrão, E., 1994. Ecozona Subtilisphaera spp.: registro eocretáceo de um importante episódio ecológico do Oceano Atlântico primitivo. Acta Geol. Leopol., XVII 39 (2), 521–538.

Arai, M., 2014. Aptian/albian (early cretaceous) paleogeography of the south Atlantic: a paleontological perspective. Braz. J. Genet. 44 (2), 339–350.

Arai, M., Assine, M.L., 2020. Chronostratigraphic constraints and paleoenvironmental interpretation of the Romualdo formation (Santana group, Araripe Basin, northeastern Brazil) based on palynology. Cretac. Res. 116, 104610.

Assine, M.L., 1990. Sedimentação e tectônica da Bacia do Araripe, Nordeste do Brasil. M. Sc. thesis. Universidade Estadual Paulista, Rio Claro.

Assine, M.L., 1992. Análise estratigráfica da bacia do Araripe, Nordeste do Brasil. Rev. Bras. Geociencias 22 (3), 289–300.

Assine, M.L., 2007. Bacia do Araripe. Bol. Geociencias Petrobras 15 (2), 371–389.

Assine, M.L., Perinotto, J.D.J., Custódio, M.A., Neumann, V.H., Varejão, F.G., Mescolotti, P.C., 2014. Sequências deposicionais do andar Alagoas da Bacia do Araripe, nordeste do Brasil. Bol. Geociencias Petrobras 22 (1), 3–28.

Assine, M.L., Quaglio, F., Warren, L.V., Simões, M.G., 2016. Comments on paper by M. Arai" Aptian/Albian (early cretaceous) paleogeography of the south Atlantic: a paleontological perspective. Braz. J. Genet. 46 (1), 3–7.

Barbosa, J.A., Hessel, M.H., Neumann, V.H., 2004. Bivalves da Formação Crato, Bacia do Araripe. Bolet. Soc. Brasil. Paleontol. 49, 41–42.

Barshad, I., 1966. The effect of a variation in precipitation on the nature of clay mineral formation in soils from acid and basic igneous rocks. In: Heller, L., Weiss, A. (Eds.), Proceedings of International Clay Conference, Israel Programme of Scientific Translation, pp. 167–173. Jerusalem, Israel.

Beurlen, K., 1962. A geologia da Chapada do Araripe. An Acad. Bras Ciências 34 (3), 365–370.

Beurlen, K., 1963. Geologia e estratigrafia da Chapada do Araripe. Sud. Tech. Rep.

Beurlen, K., 1971. As condições ecológicas e faciológicas da Formação Santana na Chapada do Araripe (Nordeste do Brasil). An Acad. Bras Ciências 43 (Suppl. ment), 411–415.

Biscaye, P.E., 1965. Mineralogy and sedimentation of recent deep-sea clay in the Atlantic Ocean and adjacent seas and oceans. Geol. Soc. Am. Bull. 76 (7), 803–832.

Bobco, F.E., Goldberg, K., Bardola, T.P., 2017. Modelo deposicional do Membro Ipubi (Bacia do Araripe, nordeste do Brasil) a partir da caracterização faciológica, petrográfica e isotópica dos evaporitos. Pesqui. em Geociencias 44 (3), 431–451.

Boucot, A., Xu, C., Scotese, C.R., Morley, R.J., 2013. Phanerozoic paleoclimate: an atlas of lithologic indicators of climate. In: Concepts in Sedimentology and Paleontology, vol. 11. Society for Sedimentary Geology, p. 478.

Brigatti, M.F., Guidotti, C.V., Malferrari, D., Sassi, F.P., 2008. Single-crystal X-ray studies of trioctahedral micas coexisting with dioctahedral micas in metamorphic sequences from western Maine. Am. Mineral. 93 (2–3), 396–408.

Brindley, G.W., Brown, G. (Eds.), 1980. Crystal Structure of Clay Minerals and Their X-Ray Identification. Mineralogical Society, London, UK, p. 504.

Campbell, F.A., Lerbekmo, J.F., 1963. Mineralogic and chemical variations between Upper Cretaceous continental Belly River shales and marine Wapiabi shales in western Alberta, Canada. Sedimentology 2 (3), 215–226.

Campbell, F.A., Williams, G.D., 1965. Chemical composition of shales of Mannville group (lower Cretaceous) of central Alberta, Canada. AAPG (Am. Assoc. Pet. Geol.) Bull. 49 (1), 81–87.

Carrado, K.A., Decarreau, A., Petit, S., Bergaya, F., Lagaly, G., 2006. Synthetic clay minerals and purification of natural clays. In: Bergaya, F., Lagaly, G. (Eds.), Handbook of Clay Science. Newnes. Developments in Clay Science, vol. 1, pp. 115–139.

Carvalho, I.S., Agnolin, F., Rolando, M.A.A., Novas, F.E., Xavier-Neto, J., Freitas, F.I., Andrade, J.A.F.G., 2019. A new genus of pipimorph frog (anura) from the early Cretaceous Crato formation (Aptian) and the evolution of South American tongueless frogs. J. S. Am. Earth Sci. 92, 222–233.

Carvalho, I.S., Leonardi, G., Rios-Netto, A.M., Borghi, L., Paula Freitas, A., Andrade, J.A., Freitas, F.I. Dinosaur trampling from the Aptian of Araripe Basin, NE Brazil, as tools for paleoenvironmental interpretation. Cretac. Res., 117, 1-13.

Carvalho, I.S., Viana, M.S.S., 1993. Os Conchostráceos da Bacia do Araripe. An Acad. Bras Ciências 65 (2), 181–187.

Catto, B., Jahnert, R.J., Warren, L.V., Varejão, F.G., Assine, M.L., 2016. The microbial nature of laminated limestones: lessons from the upper Aptian, Araripe Basin, Brazil. Sediment. Geol. 341, 304–315.

Catto, B., 2015. Laminitos Microbiais No Membro Crato (Neoaptiano), Bacia Do Araripe, Nordeste Do Brasil. M.Sc. thesis. Universidade Estadual Paulista.

Chamley, H., 1989. Clay Mineralogy. Springer, Berlin, Germany.

Cheary, R.W., Coelho, A., 1992. A fundamental parameters approach to X-ray line-profile fitting. J. Appl. Crystallogr. 25 (2), 109–121.

Chumakov, N.M., Zharkov, M.A., Herman, A.B., Doludenko, M.P., Kalandadze, N.N., Lebedev, E.A., Ponomarenko, A.G., Rautian, A.S., 1995. Climate belts of the mid cretaceous time. Stratigr. Geol. Correl. 3, 241–260.

Coimbra, J.C., Arai, M., Carreño, A.L., 2002. Biostratigraphy of lower cretaceous microfossils from the Araripe Basin, northeastern Brazil. Geobios 35 (6), 687–698.

Coimbra, R., Rocha, F., Immenhauser, A., Olóriz, F., Terroso, D., Horikx, M., 2021. Carbonate-hosted clay minerals: a critical re-evaluation of extraction methods and their possible bias on palaeoenvironmental information. Earth Sci. Rev. 103502.

Condie, K.C., 1993. Chemical composition and evolution of the upper continental crust: contrasting results from surface samples and shales. Chem. Geol. 104 (1–4), 1–37.

Craigie, N.W., 2018. Principles of Elemental Chemostratigraphy. Springer International Publishing AG, Cham, Switzerland.

Cullers, R.L., 2002. Implications of elemental concentrations for provenance, redox conditions, and metamorphic studies of shales and limestones near Pueblo, CO, USA. Chem. Geol. 191 (4), 305–327.

Cullers, R.L., Podkovyrov, V.N., 2002. The source and origin of terrigenous sedimentary rocks in the Mesoproterozoic Ui group, southeastern Russia. Precambrian Res. 117 (3–4), 157–183.

Dino, R., 1992. Palinologia, bioestratigrafia e paleoecologia da Formação Alagamar-Cretáceo da bacia Potiguar. Nordeste do Brasil. Ph.D. thesis, Universidade de São Paulo.

Duarte, G., Borghi, L., 2018. Petrografia das Fácies Evaporíticas Sulfatadas do Membro Ipubi, Formação Santana (Bacia do Araripe). Anu. do Inst. Geociencias 41 (2), 606–613.

Floyd, P.A., Leveridge, B.E., 1987. Tectonic environment of the Devonian Gramscatho basin, south Cornwall: framework mode and geochemical evidence from turbiditic sandstones. J. Geol. Soc. 144 (4), 531–542.

Folk, R.L., 2002. Petrology of Sedimentary Rocks. Hemphill publishing company.

Galarraga, F., Reategui, K., Martïnez, A., Martínez, M., Llamas, J.F., Márquez, G., 2008. V/Ni ratio as a parameter in palaeoenvironmental characterisation of nonmature medium-crude oils from several Latin American basins. J. Petrol. Sci. Eng. 61 (1), 9–14.

Geiger, M., 2010. The geology of the southern Warmbad Basin margin-Tephrostratigraphy, age, fossil record and sedimentary environment of Carboniferous-Permian glacigenic deposits of the Dwyka Group, Zwartbas, southern Namibia. Ph.D. thesis (Julius-Maximilians-Universität).

Goldberg, K., Premaor, E., Bardola, T., Souza, P.A., 2019. Aptian marine ingression in the Araripe Basin: implications for paleogeographic reconstruction and evaporite accumulation. Mar. Petrol. Geol. 107, 214–221.

Goodyear, J., Duffin, W.J., 1961. An X-ray examination of an exceptionally well crystallized kaolinite. Mineral. Mag. J. Mineral Soc. 32 (254), 902–907.

Hay, W.W., Floegel, S., 2012. New thoughts about the Cretaceous climate and oceans. Earth Sci. Rev. 115 (4), 262–272.

Heimhofer, U., Ariztegui, D., Lenniger, M., Hesselbo, S.P., Martill, D.M., Rios-Netto, A. M., 2010. Deciphering the depositional environment of the laminated Crato fossil beds (early cretaceous, Araripe Basin, north-eastern Brazil). Sedimentology 57 (2), 677–694.

Holanda, W., dos Santos, A.C., Bertolino, L.C., Bergamaschi, S., Rodrigues, R., da Costa, D.F., Jones, C.M., 2019. Paleoenvironmental, paleoclimatic and stratigraphic implications of the mineralogical content of the Irati Formation, Paraná Basin, Brazil. J. S. Am. Earth Sci. 94, 102243.

International Centre for Diffraction Data PDF4+ (ICDD), 2012, (Newton Square, USA).

Jones, B., Manning, D.A., 1994. Comparison of geochemical indices used for the interpretation of palaeoredox conditions in ancient mudstones. Chem. Geol. 111 (1–4), 111–129.

Keller, W.D., 1978. Classification of kaolins exemplified by their textures in scan electron micrographs. Clay Clay Miner. 26 (1), 1–20.

Kern, A., Eysel, W., 1993. Mineralogisch-Petrograph. Institute, University of Hidelberg, Germany (ICDD Grant-in-Aid).

Lima, M.R.D., 1978. Palinologia da Formação Santana (Cretáceo do Nordeste do Brasil. Ph.D. thesis. Universidade de São Paulo.

Lima, M.R.D., 1983. Paleoclimatic reconstruction of the Brazilian Cretaceous based on palynological data. Rev. Bras. Geociencias 13 (4), 223–228.

Lucio, T., 2017. Geocronologia, geoquímica isotópica Re-Os e elemental em folhelhos pirobetuminosos da Formação Ipubi, Bacia do Araripe. M.Sc. thesis Univ. Fed. Pernambuco.

Lúcio, T., Neto, J.A.S., Selby, D., 2020. Late Barremian/early Aptian Re–Os age of the Ipubi formation black shales: stratigraphic and paleoenvironmental implications for Araripe Basin, northeastern Brazil. J. S. Am. Earth Sci. 102699.

Martill, D.M., Bechly, G., Loveridge, R.F., 2007a. The Crato Fossil Beds of Brazil: Window into an Ancient World. Cambridge University Press.

Martill, D.M., Loveridge, R., Heimhofer, Ulrich, 2007b. Halite pseudomorphs in the Crato formation (early cretaceous, late Aptian-early Albian), Araripe Basin, northeast Brazil: further evidence for hypersalinity. Cretac. Res. 28, 613–620.

Martill, D.M., Wilby, P.R., 1993. Stratigraphy. In: Martill, D.M. (Ed.), *Fossils Of the Santana And Crato Formations, Brazil*. Field Guides to Fossils, 5. The Palaeontological Association, London.

McKirdy, D.M., Hall, P.A., Nedin, C., Halverson, G.P., Michaelsen, B.H., Jago, J.B., Gehling, J.G., Jenkins, R.J.F., 2011. Paleoredox status and thermal alteration of the lower cambrian (series 2) emu Bay shale lagerstätte, south Australia. Aust. J. Earth Sci. 58 (3), 259–272.
McLennan, S.M., 2001. Relationships between the trace element composition of sedimentary rocks and upper continental crust. G-cubed 2 (4).
McLennan, S.M., Hemming, S., McDaniel, D.K., Hanson, G.N., 1993. Geochemical Approaches to Sedimentation, Provenance, and Tectonics. Special Papers-Geological Society of America, p. 21, 21.
McLennan, S.M., Taylor, S.R., 1991. Sedimentary rocks and crustal evolution: tectonic setting and secular trends. J. Geol. 99 (1), 1–21.
Meunier, A., 2005. Clays. Springer Science & Business Media.
Moore, D.M., Reynolds Jr., R.C., 1997. X-ray Diffraction and the Identification and Analysis of Clay Minerals. Oxford University Press (OUP).
Munsell, 2009. Geological Rock-Color Chart. Geological Society of America (GSA).
Nesbitt, H.W., Young, G.M., 1984. Prediction of some weathering trends of plutonic and volcanic rocks based on thermodynamic and kinetic considerations. Geochem. Cosmochim. Acta 48 (7), 1523–1534.
Neumann, V.H.D.M.L., 1999. Estratigrafia, sedimentologia, geoquímica y diagenesis de los Sistemas Lacustres Aptiense-Albienses de la Cuenca de Araripe (Noreste de Brasil). Ph.D. thesis. Universitat de Barcelona.
Neumann, V.H., Cabrera, L., 2002. Características hidrogeológicas gerais, mudanças de salinidade e caráter endorréico do sistema lacustre cretáceo do Araripe, NE Brasil. Rev. Geol. 15, 43–54.
Paula-Freitas, A.B.L., Borghi, L., 2010. Análise estratigráfica do intervalo siliciclástico Aptiano da Bacia do Araripe (Formação Rio da Batateira). M.Sc. thesis. Universidade Federal do Rio de Janeiro.
Petri, S., 1983. Brazilian Cretaceous paleoclimates: evidence from clay-minerals, sedimentary structures and palynomorphs. Rev. Bras. Geociencias 13 (4), 215–222.
Ponte, F.C., Appi, C.J., 1990. Proposta de revisão da coluna litoestratigráfica da Bacia do Araripe. Congr. Brasil. Geol. 36, 211–226.
Pourmand, A., Dauphas, N., Ireland, T.J., 2012. A novel extraction chromatography and MC-ICP-MS technique for rapid analysis of REE, Sc and Y: revising CI-chondrite and Post-Archean Australian Shale (PAAS) abundances. Chem. Geol. 291, 38–54.
Regali, M.S.P., 1990. Biocronoestratigrafia e paleoambiente do Eocretáceo das bacias do Araripe (CE) e Rio do Peixe (PB), NE-Brasil. Simpósio Sobre a Bacia do Araripe e Bacias Interior. Nordeste 1, 163–172.
Rego, E.S., Jovane, L., Hein, J.R., Sant'Anna, L.G., Giorgioni, M., Rodelli, D., Özcan, E., 2018. Mineralogical evidence for warm and dry climatic conditions in the Neo-Tethys (eastern Turkey) during the middle Eocene. Palaeogeogr. Palaeoclimatol. Palaeoecol. 501, 45–57.
Ribeiro, A.C., Ribeiro, G.C., Varejão, F.G., Battirola, L.D., Pessoa, E.M., Simões, M.G., Warren, L.V., Riccomini, C., Poyato-Ariza, F.J., 2021. Towards an actualistic view of the Crato Konservat-Lagerstätte paleoenvironment: a new hypothesis as an Early Cretaceous (Aptian) equatorial and semi-arid wetland. Earth Sci. Rev. 103573.
Rios-Netto, A.M., 2011. Evolução paleoambiental e palinoestratigrafia do intervalo Alagoas na parte oriental da Bacia do Araripe, Nordeste do Brasil. Ph.D. Thesis Univ. Fed. Rio de Janeiro.
Rios-Netto, A.M., Paula-Freitas, A.B.L., Carvalho, I.S., Regali, M.S.P., Borghi, L., Freitas, F.I., 2012a. Formalização estratigráfica do Membro Fundão, Formação Rio da Batateira, Cretáceo Inferior da Bacia do Araripe. Nordeste do Brasil.
Rios-Netto, A.M., Regali, M.D.S.P., Carvalho, I.S., Freitas, F.I., 2012b. Palinoestratigrafia do intervalo Alagoas da Bacia do Araripe, Nordeste do Brasil. Rev. Bras. Geociencias 42 (2), 331–342.
Sá, J.M., McReath, I., Leterrier, J., 1995. Petrology, geochemistry and geodynamic setting of Proterozoic igneous suites of the Orós fold belt (Borborema Province, Northeast Brazil). J. S. Am. Earth Sci. 8 (3–4), 299–314.
Santos, H.N., Neumann, R., Ávilla, C.A., 2017. Mineral quantification with simultaneous refinement of Ca-Mg carbonates non-stoichiometry by X-ray diffraction. Rietveld Method. Miner. 7 (9), 164.
Sari, A., Koca, D., 2012. Jura - kretase yaşlı Akkuyu Formasyonunun (Orta Toroslar/Türkiye) provenans, tektonik ve redoks koşullarına bir yaklaşım. Maden Tetkik ve Arama Dergisi, Sayı 144, 51–73.
Scherer, C.M., Goldberg, K., Bardola, T., 2015. Facies architecture and sequence stratigraphy of an early post-rift fluvial succession, Aptian Barbalha Formation, Araripe Basin, northeastern Brazil. Sediment. Geol. 322, 43–62.
Silva, L.D., McNaughton, N.J., Vasconcelos, A.M., Gomes, J.R.C., Fletcher, I.R., 1997. U-Pb SHRIMP ages in southern state of Ceará, Borborema Province, NE Brazil: Archean TTG accretion and proterozoic crustal reworking. In: Second International Symposium on Granites and Associated Mineralizations. Salvador, Brazil, p. 280.
Silvestre, D.D.C., 2017. Análise faciológica e caracterização de sistemas deposicionais da Formação Barbalha (Aptiano Superior) – Bacia do Araripe. Master thesis. Universidade Federal de Pernambuco.
Singer, A., 1984. The paleoclimatic interpretation of clay minerals in sediments—a review. Earth Sci. Rev. 21 (4), 251–293.
Storari, A.P., Rodrigues, T., Bantim, R.A., Lima, F.J., Saraiva, A.A., 2021. Mass mortality events of autochthonous faunas in a lower cretaceous gondwanan lagerstätte. Sci. Rep. 11 (1), 1–11.
Taylor, S.R., McLennan, S.M., 1985. The Continental Crust: its Composition and Evolution (United States).
Technisch Physiscge Dienst, 1966. ICDD Graint-in-Aid, Delft, The Netherlands.
Teles, M.S.L., Berthou, P., 1995. Estudo dos argilominerais das Bacias do Araripe, Rio do Peixe, Barro e Padre Marcos no Nordeste do Brasil e geoquímica orgânica das Formações Santana e Rio da Batateira na Bacia do Araripe. M.Sc. thesis. Universidade Federal do Rio de Janeiro.
Thiry, M., 2000. Palaeoclimatic interpretation of clay minerals in marine deposits: an outlook from the continental origin. Earth Sci. Rev. 49 (1–4), 201–221.
Tobia, F.H., Mustafa, B.H., 2016. Geochemistry and mineralogy of the Al-rich shale from Baluti Formation, Iraqi Kurdistan region: implications for weathering and provenance. Arab. J. Geosci. 9 (20), 757.
USGS, 2006. FGDC Digital Cartographic Standard for Geologic Map Symbolization (PostScript Implementation) (Technical report).
Vale, J.A.R., 2018. Caracterização geoquímica e geocronológica do Complexo Granjeiro Sul, Província Borborema, NE Brasil: implicações para a evolução crustal paleoarqueana do distrito ferrífero de Curral Novo do Piauí. Ph.D. thesis. Universidade de São Paulo.
Varejão, F.G., Warren, L.V., Simões, M.G., Buatois, L.A., Mángano, M.G., Bahniuk, A.M., Assine, M.L., 2021a. Mixed siliciclastic-carbonate sedimentation in an evolving epicontinental sea: Aptian record of marginal marine settings in the interior basins of north-eastern Brazil. Sedimentology.
Varejão, F.G., Silva, V.R., Assine, M.L., Warren, L.V., Matos, S.A., Rodrigues, M.G., Fursich, F.T., Simões, M.G., 2021b. Marine or freshwater? Accessing the paleoenvironmental parameters of the Caldas bed, a key marker bed in the Crato formation (Araripe Basin, NE Brazil). Brazil. J. Geol. 51 (1), 1–12.
Verma, S.P., Armstrong-Altrin, J.S., 2013. New multi-dimensional diagrams for tectonic discrimination of siliciclastic sediments and their application to Precambrian basins. Chem. Geol. 355, 117–133.
Viani, A., Gualtieri, A.F., Artioli, G., 2002. The nature of disorder in montmorillonite by simulation of X-ray powder patterns. Am. Mineral. 87 (7), 966–975.
Visser, J.N., Young, G.M., 1990. Major element geochemistry and paleoclimatology of the Permo-Carboniferous glacigene Dwyka Formation and postglacial mudrocks in southern Africa. Palaeogeogr. Palaeoclimatol. Palaeoecol. 81 (1–2), 49–57.
Warr, L.N., 2020. Recommended abbreviations for the names of clay minerals and associated phases. Clay Miner. 1–4.
Weaver, C.E., 1989. Clays, Muds, and Shales. Elsevier, United States.
Whitney, D.L., Evans, B.W., 2010. Abbreviations for names of rock-forming minerals. Am. Mineral. 95 (1), 185–187.
Young, R.A., 1993. The Rietveld Method, vol. 5, pp. 1–38.